

The Sphere of Influence of the Bright Central Galaxies in the Diffuse Light of SDSS Clusters

Xiaokai Chen¹, Ying Zu^{1,2*}, Zhiwei Shao¹, Huanyuan Shan^{3,4}

¹Department of Astronomy, School of Physics and Astronomy, Shanghai Jiao Tong University, Shanghai 200240, China

²Shanghai Key Laboratory for Particle Physics and Cosmology, Shanghai Jiao Tong University, Shanghai 200240, China

³Shanghai Astronomical Observatory (SHAO), Nandan Road 80, Shanghai 200030, China

⁴University of Chinese Academy of Sciences, Beijing 100049, China

Accepted XXX. Received YYY; in original form ZZZ

ABSTRACT

The bright central galaxies (BCGs) dominate the inner portion of the diffuse cluster light, but it is still unclear where the intracluster light (ICL) takes over. To investigate the BCG-ICL transition, we stack the images of ~ 3000 clusters between $0.2 < z < 0.3$ in the SDSS *gri* bands, and measure their BCG+ICL stellar surface mass profile Σ_*^{B+I} down to $3 \times 10^4 M_\odot/\text{kpc}^2$ at $R \approx 1 \text{ Mpc}$ ($\sim 32 \text{ mag/arcsec}^2$ in the *r*-band). We develop a physically-motivated method to decompose Σ_*^{B+I} into three components, including an inner de Vaucouleurs' profile, an outer ICL that follows the dark matter distribution measured from weak lensing, and an intriguing transitional component between 70 and 200 kpc. To investigate the origin of this transition, we split the clusters into two subsamples by their BCG stellar mass M_*^{BCG} (mass enclosed roughly within 50 kpc) while making sure they have the same distribution of satellite richness. The Σ_*^{B+I} profiles of the two subsamples differ by more than a factor of two at $R < 50 \text{ kpc}$, consistent with their 0.34 dex difference in M_*^{BCG} , whereas on scales beyond 400 kpc the two profiles converge to the same amplitudes, suggesting a satellite-stripping origin of the outer ICL. Remarkably, however, the discrepancy between the two Σ_*^{B+I} profiles persist at above 50% level on all scales below 200 kpc, thereby revealing the BCG sphere of influence with radius $R_{\text{SOI}} \approx 200 \text{ kpc}$. Finally, we speculate that the surprisingly large sphere of influence of the BCG is tied to the elevated escape velocity profile within r_s , the characteristic radius of the dark matter haloes.

Key words: galaxies: evolution — galaxies: formation — galaxies: abundances — galaxies: statistics — cosmology: large-scale structure of Universe

1 INTRODUCTION

The intracluster light (ICL) is primarily produced by stray stars that have escaped individual galaxies but remain gravitationally bound to the cluster potential (Zwicky 1937; de Vaucouleurs & de Vaucouleurs 1970; Welch & Sastry 1971; Melnick, White, & Hoessel 1977; Feldmeier et al. 2004; Mihos et al. 2005; Krick & Bernstein 2007). As the by-product of galaxy interactions within clusters (for a recent review; see Contini 2021), these free-floating stars are key to unlocking the assembly history of the bright central galaxies (BCGs¹) with future deep imaging surveys like LSST (Rubin; Ivezić et al. 2019), Euclid (Laureijs et al. 2011), Roman (Spergel et al. 2015), and the Chinese Survey Space Telescope (CSST; Gong

et al. 2019). However, it is unclear whether there exists an ICL component that is physically distinct from the diffuse stellar envelope of the BCG (Kormendy & Bahcall 1974), and if so, where the ICL begins and the sphere of influence of the BCG ends (Doherty et al. 2009). In this paper, we examine the BCG+ICL stellar surface mass profile Σ_*^{B+I} of a large sample of clusters observed by the Sloan Digital Sky Survey (SDSS; York et al. 2000), in hopes of finding a more physically-motivated method of decomposing the Σ_*^{B+I} profile and the BCG “sphere of influence” within the diffuse cluster light.

In hydrodynamical simulations, methods for kinematically decomposing BCG vs. ICL have been developed based on the apparent bimodal distribution of the intracluster stellar velocities (Dolag et al. 2010; Cui et al. 2014). However, such exquisite methods developed for simulations are not applicable in the observations of distant clusters where stellar velocities are inaccessible (but see Arnaboldi et al. 1996; Romanowsky et al. 2012; Longobardi et al. 2015; Spinelli et al. 2018; Gu et al. 2020, for kinematic studies of ICL in local clusters). As a result, traditional methods of decomposition usually

* E-mail: yingzu@sjtu.edu.cn

¹ We do not conform to the more commonly-adopted nomenclature of “brightest cluster galaxies”, because the BCGs in this work are likely the central galaxies but not necessarily the brightest.

assume that the diffuse light below some arbitrary surface brightness (SB) limit belongs to the ICL (Rudick et al. 2011; Burke et al. 2012; Presotto et al. 2014; Tang et al. 2018; Furnell et al. 2021), or describe the BCG+ICL SB profile μ^{B+I} as the sum of multiple Sérsic components (Gonzalez et al. 2005; Seigar et al. 2007; Donzelli et al. 2011; Cooper et al. 2015; Zhang et al. 2019; Montes et al. 2021; Kluge et al. 2021). Despite the incoming deep photometric dataset from LSST+*Euclid*+*Roman*+CSST, a well-defined physical decomposition of the BCG+ICL profile is still lacking.

Recently, several studies proposed that the ICL in the outer region of clusters should follow the distribution of dark matter, due to the fact that the stray stars and dark matter particles are both collisionless tracers of the cluster potential (Montes & Trujillo 2019; Alonso Asensio et al. 2020; Contini & Gu 2020; Sampaio-Santos et al. 2021). By the same token, the outer ICL may also follow the distribution of satellite galaxies, whose mass loss contributes significantly to the ICL (Purcell et al. 2007; Martel et al. 2012; Contini et al. 2014; Morishita et al. 2017). In this paper, we not only measure the BCG+ICL stellar surface mass density profile Σ_*^{B+I} from image stacking, but also the total surface mass density profile Σ_m from cluster weak lensing, as well as the galaxy surface number density profile Σ_g from cluster-galaxy cross-correlation functions. By comparing the Σ_*^{B+I} profile with Σ_m and Σ_g , we develop a physically-motivated method for the decomposition of the diffuse cluster light without resorting to arbitrary SB limits or multiple Sérsic profiles.

In theory, since the intracluster stars are unlikely born *in situ* (Puchwein et al. 2010; Melnick et al. 2012), the build-up of the diffuse light should be closely linked to the dynamical evolution of the BCG and satellite galaxies, including: (1) mergers of satellites with the BCG (Murante et al. 2007; Burke et al. 2015), (2) tidal disruption/stripping of satellites in the central region of the cluster (Purcell et al. 2007; Wetzel & White 2010; Montes & Trujillo 2014; DeMaio et al. 2015; Contini et al. 2018), (3) tidal and ram-pressure stripping of infalling satellites (Rudick et al. 2009; Contini et al. 2014; Montes & Trujillo 2018; DeMaio et al. 2018; Contini et al. 2019; Jiménez-Teja et al. 2018), and (4) pre-processing within infalling groups (Willman et al. 2004; Sommer-Larsen 2006; Rudick et al. 2006). Among these processes, (1) and (2) can simultaneously grow the BCG *and* the ICL within a Hubble time, while (3) and (4) deposit stars only into the ICL without growing the BCG. In particular, the amount of ICL growth through (1) and (2) should be strongly correlated with the observed BCG stellar mass M_*^{BCG} , but the ICL growth induced by (3) and (4) would be tied instead to the number of satellite galaxies within the cluster (a.k.a., cluster richness λ).

Therefore, any physically meaningful decomposition should reveal at least two distinct components of the diffuse cluster light, one *BCG-induced* and the other *richness-induced*. Obviously, the radial extent of the BCG-induced portion can be regarded as the radius of the BCG sphere of influence R_{SOI} within the diffuse cluster light. In this paper, we divide clusters into high and low- M_*^{BCG} subsamples at fixed λ (see also Zu et al. 2021, hereafter referred to as Z21), and infer R_{SOI} by comparing the Σ_*^{B+I} profiles between the two subsamples. Using weak lensing, Z21 found that the average halo concentration of the high- M_*^{BCG} clusters is $\sim 10\%$ higher than that of the low- M_*^{BCG} clusters, but their average halo masses are the same. Since the two populations have the same λ (and average halo mass) but differ only in M_*^{BCG} , we expect their $\Sigma_*^{B+I}(R)$ profiles to have equal richness-induced contributions beyond R_{SOI} , but exhibit distinct levels of BCG-induced diffuse mass below R_{SOI} — a potentially smoking-gun detection of R_{SOI} .

This paper is organised as follows. We provide an overview of the cluster catalogue and photometric images in §2, setting the stage for our BCG+ICL SB profile measurement pipeline in §3. We describe the measurement and the decomposition of the BCG+ICL stellar surface density profile Σ_*^{B+I} in §4, and then present the observational detection of the BCG sphere of influence in §5. We conclude by summarizing our findings and looking to the future in §6. Throughout the paper, we assume the Planck (2016) cosmology ($\Omega_m=0.31$, $\sigma_8=0.816$, $h=0.677$), and convert all distances into physical coordinates. We use $\lg x = \log_{10} x$ for the base-10 logarithm and $\ln x = \log_e x$ for the natural logarithm.

2 DATA

2.1 Cluster Catalogue

Following Z21, we employ the SDSS redMaPPer cluster catalogue (Rykoff et al. 2014) derived by applying a red sequence-based cluster finding algorithm to the SDSS DR8 imaging (Aihara et al. 2011). Briefly, redMaPPer iteratively self-trains a model of red-sequence galaxies calibrated by an input spectroscopic galaxy sample, and then attempts to grow a galaxy cluster centred about each photometric galaxy. Once a galaxy cluster has been identified by the matched-filters, the algorithm iteratively solves for a photometric redshift based on the calibrated red-sequence model, and re-centres the clusters about the best BCG candidates with the highest probability of being the central galaxy p_{cen} (Rykoff et al. 2014).

For each detected cluster, redMaPPer applies an aperture of $\sim 1 h^{-1} \text{Mpc}$ (with a weak dependence on richness λ), and assign each galaxy within the aperture a membership probability p_{mem} . The satellite richness λ was computed by summing the p_{mem} of all member galaxy candidates, which roughly corresponds to the number of red-sequence satellite galaxies brighter than $0.2 L_*$. At $\lambda \geq 20$, the SDSS redMaPPer cluster catalogue is approximately volume-complete up to $z \approx 0.33$, with cluster photometric redshift uncertainties as small as $\delta(z) = 0.006/(1+z)$. We select 4593 clusters with $\lambda \geq 20$ and redshifts between 0.2 and 0.3 ($\langle z \rangle = 0.254$). The maximum redshift of 0.3 is primarily set by the requirement of sample completeness, and partly because the cosmic dimming effect renders the detection of low-SB signals within SDSS challenging at the higher redshift ($\mu \propto (1+z)^{-4}$).

We pick the galaxy with the highest p_{cen} in each cluster as the BCG, and derive an *i*-band cModel magnitude-based stellar mass M_*^{BCG} for each BCG. In general, the SDSS model magnitudes are preferred for measuring the color of extended objects like the BCGs (hence a better mass-to-light ratio indicator), because flux is measured consistently through the same aperture across all bands, while the cModel magnitudes provide a more robust estimate of the total flux based on independent model fits in each bandpass (but see Bernardi 2017). Therefore, we rescale the extinction-corrected *gri* model magnitudes to the *i*-band cModel magnitudes, and fit a Stellar Population Synthesis (SPS) model to the scaled *gri* magnitudes to infer M_*^{BCG} .

Following Maraston et al. (2009), we assume a simultaneous burst of two Simple Stellar Populations (SSPs) at the same epoch, one dominant stellar population (97 per cent) with solar metallicity and the other a secondary (3 per cent) metal-poor ($Z=0.008$) population. We utilize the EzGal software (Mancone & Gonzalez 2012) and adopt the BC03 SSP model and the Chabrier IMF for the fits. For a detailed comparison between our photometric stellar

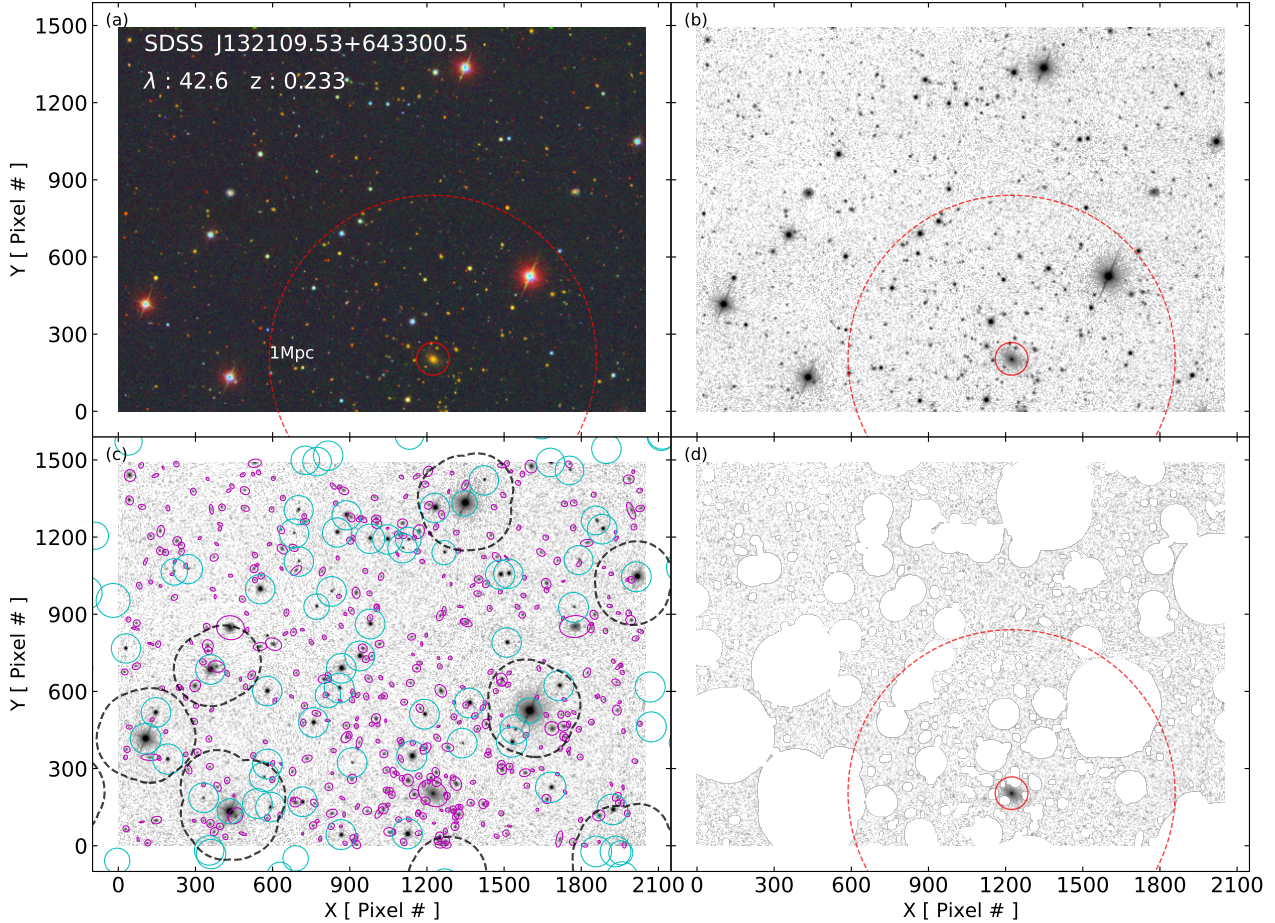


Figure 1. Example of star and galaxy masks on the standard SDSS image frame ($589 \times 811 \text{ arcsec}^2$) of a cluster with $\lambda = 42.6$ at $z = 0.233$. The image dimension is 2048×1489 pixels, and the white margin area between the image frame and the panel edge has a width of 100 pixels. Panel (a): SDSS *gri*-band composite image of the cluster, with its BCG indicated by the inner solid circle with a radius of 100 kpc. The outer dashed circle indicates the cluster region of 1 Mpc radius. Panel (b): The SDSS *r*-band image frame. Panel (c): Cyan circles and magenta ellipses are the star and galaxy masks, respectively, while the regions delineated by black dashed lines are the merged masks of saturated pixels surrounding bright stars. Note that we also include the masks of sources that are centred in the white margin area (i.e., outside but close to the image frame), as they could still pollute the pixels inside the image frame. Panel (d): Final masked image that only includes the light from the BCG, ICL, and unmasked sources that are below the detection threshold.

mass estimates and the spectroscopic stellar masses from [Chen et al. \(2012\)](#), we refer interested readers to the Figure 1 in [Z21](#).

Due to the magnitude rescaling, our estimates of M_*^{BCG} should inherit the effective aperture of the *i*-band cModel magnitudes. By examining the stacked surface stellar mass density profiles of clusters at fixed M_*^{BCG} but different λ (as will be demonstrated later in §5), we find that the effective aperture of our M_*^{BCG} estimates is $R_* \approx 50 \text{ kpc}$. Therefore, our fiducial M_*^{BCG} roughly corresponds to $M_{*,50\text{kpc}}$ in the language of [Huang et al. \(2021\)](#). To test the robustness of our R_{SOI} detection, we also measure for each BCG an aperture-based stellar mass $M_{*,20\text{kpc}}$, i.e., stellar mass enclosed within a fixed aperture of 20 kpc.

2.2 SDSS Images

For any given set of clusters, we stack their SDSS images centred on the BCGs and measure the average 1D SB profile from the stacked 2D image. In this paper, we employ the observed images derived from the SDSS DR8, the same imaging data from which the `redMaPPer` cluster catalogue was built. The images were

processed with the latest SDSS photometric pipeline `photo v5_6`, which implements an updated sky subtraction method that significantly improves the flux estimates for bright objects, detection of faint objects around bright objects, and extended light measurement of large objects ([Blanton et al. 2011](#)). In particular, we make use of the ‘‘corrected frames’’, i.e., the calibrated and sky-subtracted images (with bad columns and cosmic rays interpolated over) in the *g*, *r*, and *i* bands. Each corrected frame has a dimension of 2048 pixels \times 1489 pixels, which corresponds to a sky area of $13.5 \times 9.8 \text{ arcmin}^2$ (the pixel size is 0.396 arcsec). The improved photometric reduction of the SDSS images allows a robust measurement of the large-scale, diffuse light distribution within massive clusters, which was severely underestimated in the previous SDSS photometric pipeline ([Bernardi et al. 2013; Kravtsov et al. 2018](#)).

We apply a two-step procedure to identify the defect images that could severely corrupt the low-surface brightness signal. In the first step, we perform visual inspection of each image to look for strong defects that could severely undermine the stacked signal across all scales, e.g., extremely bright stars (and their extended bright wings) and strong cosmic rays across the frame. In the second

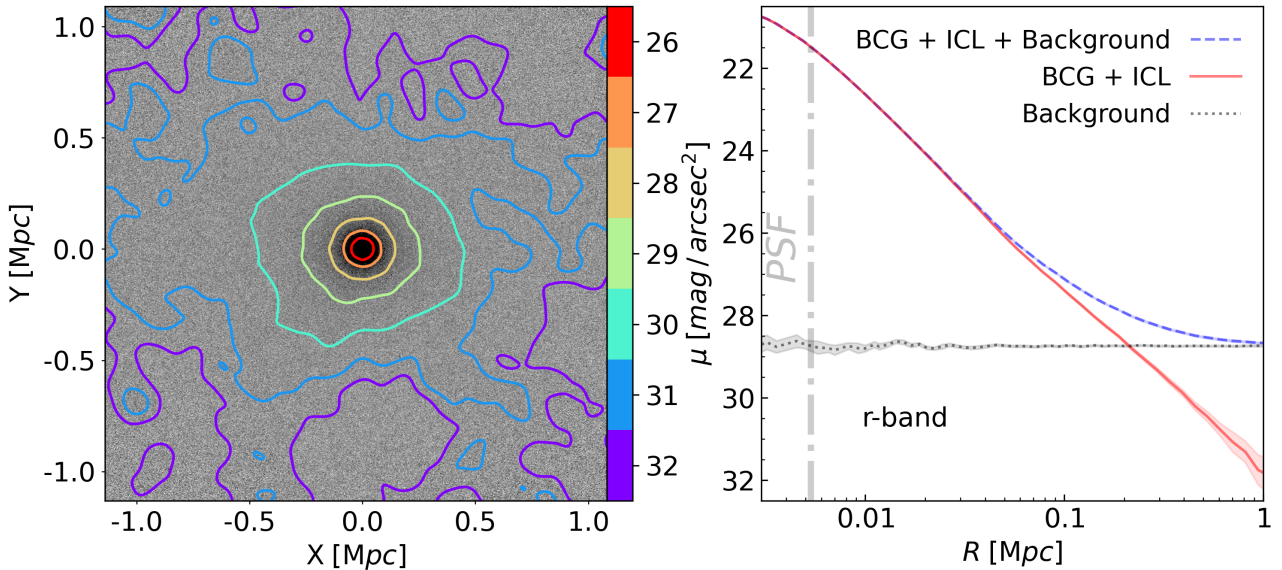


Figure 2. *Left:* r -band stacked image of the BCG+ICL light of our overall cluster sample (grayscale). Contour lines indicate seven levels of SB ranging from 26 to 32 $\text{mag}/\text{arcsec}^2$ with $\Delta\mu=1 \text{ mag}/\text{arcsec}^2$, colour-coded by the vertical colourbar on the right. Smoothing kernels of 3, 7, 11, 17, 29, 29, and 29 pixels are applied to the seven contour levels, respectively. *Right:* SB profiles of the BCG+ICL signal (red solid), background (gray dotted), and the sum of the signal and background (blue dashed). Shaded band centred on each curve represents the 1σ uncertainties estimated from Jackknife resampling. Dot-dashed vertical line indicates the physical scale that the PSF size corresponds to at $z=0.25$.

step, we develop a simple σ -clipping scheme to reject some mildly defective images that could still impair our capability of detecting the faint ICL on scales larger than a few hundred kpc. In particular, we divide each image frame (after masking out all the galaxies, bright stars, and saturated pixels; described further below) into approximately 70 square patches with side length of 200 pixels, and measure the average pixel flux (\bar{f}_{pat}) within each patch. In addition, we measure the mean (\bar{f}_{img}) and scatter (σ) of the average fluxes of the 70 patches, and compute the deviation of the average flux of each patch from the mean flux of the entire image as $\Delta f \equiv |\bar{f}_{\text{pat}} - \bar{f}_{\text{img}}|$. We consider any image that includes a large block of M connected patches with $\Delta f > N\sigma$ to be a potential contaminant. After extensive convergence tests, we find that the combination of $M=5$ and $N=6$ provides a robust selection criteria for culling out bright extended features of non-cluster origin. In total, we identify 1466 strongly and 1690 mildly defective images of the 4593 clusters from all three bands and exclude them from further stacking analysis, leaving 2898 clusters within our final sample.

3 SURFACE BRIGHTNESS PROFILE

To measure the SB profiles of the BCG+ICL μ^{B+I} , we mask out the stars and non-BCG galaxies (i.e., satellites and background galaxies) from each image, and then transform all the images from the cluster redshifts to the same reference redshift of $z_{\text{ref}}=0.25$ (with the same pixel size but different image sizes).

Our method for image stacking is largely similar to that of (Zibetti et al. 2005, hereafter referred to as Z05), but with three important distinctions. Firstly, we directly utilize the sky-subtracted corrected frames for our SB measurements, while Z05 performed an independent sky subtraction on images in the SDSS Early Data Release. We have tested the Z05 sky-subtraction method on the raw DR8 SDSS images and find that the Z05 method generally

produces consistent results compared to the SDSS pipeline. Secondly, we estimate the background level of the SB profiles, primarily due to undetected background galaxies and foreground stars, by stacking the real SDSS images centred on the coordinates of redMaPPer random clusters, while Z05 inferred the background SB by extrapolating from the best-fitting projected Navarro-Frenk-White (NFW; Navarro, Frenk, & White 1997) profile of the SB measurement below 900 kpc. Lastly, we estimate the error matrix of our SB profiles by resampling the cluster sample into 30 Jackknife samples (described further below), while Z05 divided the annulus at each radius into N angular sectors and calculated the error on the mean SB as the rms of the N SB values divided by $\sqrt{N-1}$. We find that the diagonal errors from our Jackknife error matrix is generally larger than the Z05 errors by a factor of two on scales above 10 kpc, likely because the SB of neighboring sectors within the same annulus are highly correlated. We describe each step of our SB measurement in turn below.

3.1 Image Masking

For any star brighter than $m_r=20$ and has the full width at half maximum (FWHM) measured in at least one of the other two bands, we adopt the maximum FWHM of the three bands and multiply it by 30 as the diameter of its mask. We further increase the diameter of the masks to $75 \times \text{FWHM}$ for the saturated pixels. For stars detected only in r band or fainter than $m_r=20$, we leave them unmasked in the image but will remove their light statistically through background subtraction. We have extensively tested the impact of different mask sizes on the measured BCG+ICL SB profile, and verified that our choices yield the best combination of signal-to-noise ratio (S/N) and star light mitigation.

For galaxy masks, we run SExtractor (Bertin & Arnouts 1996) on the cluster images in three bands separately, using a de-

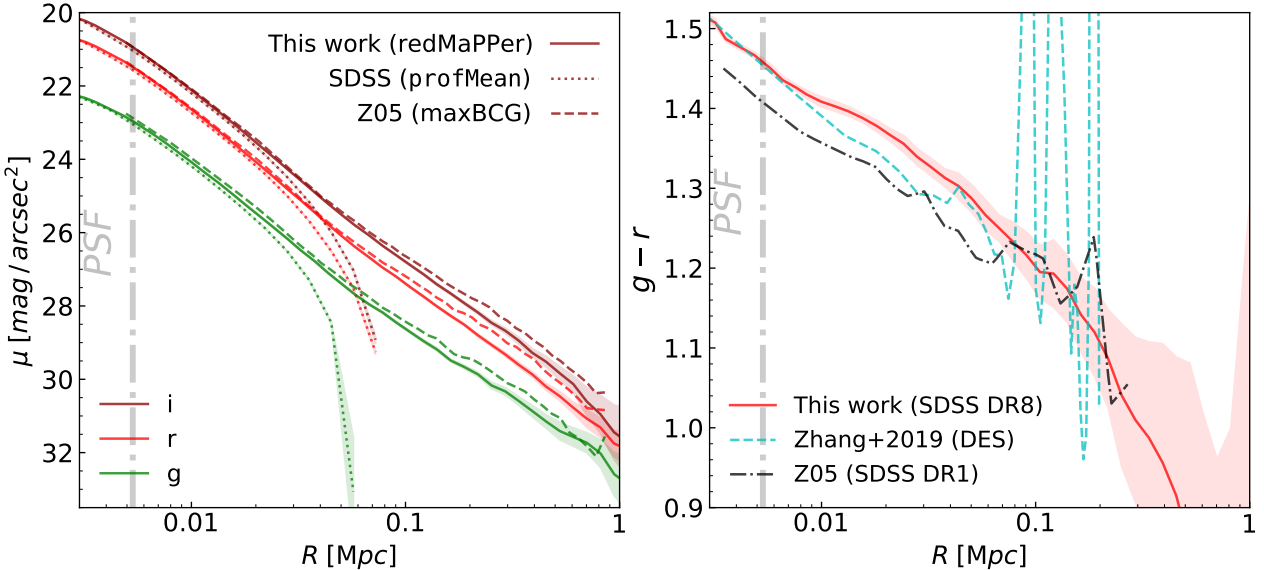


Figure 3. Comparison of our measurements of the BCG+ICL SB (left) and colour (right) profiles with previous studies. *Left:* Solid, dashed, and dotted curves indicate the BCG+ICL SB profiles from our measurements for redMaPPer clusters, Z05 for maxBCG clusters, and the SDSS photometric pipeline (profMean) for the redMaPPer BCGs, respectively. Green, red, and maroon curves are the measurements for the g , r , i bands, respectively. *Right:* Red solid, cyan dashed, and black dot-dashed curves indicate the BCG+ICL colour profiles measured by our work from SDSS DR8, Z05 from SDSS DR1, and Zhang et al. (2019) from DES, respectively. In both panels, the dot-dashed vertical lines indicate the scale of the PSF, and the shaded bands around the solid curves represent the 1σ uncertainties estimated from Jackknife resampling.

tection threshold of 1.5σ and a minimum detection area of five pixels. Such detection criteria result in a limiting magnitude of roughly 22.08 magnitude in the i band (i.e., an absolute magnitude of -18.49 for a galaxy at $z=0.25$). We multiply the semi-major and semi-minor radii of the ellipses detected by SExtractor both by a factor of eight, and adopt the augmented ellipses as the masks for galaxies. We include the BCGs in the masks for the image selection described in §2.2, but leave them unmasked in the stacked profile measurements. The factor of eight is a relatively conservative choice, which ensures that we remove almost all the light from galaxy outskirts and the scattered light from some of the very bright, nearby galaxies.

To further remove any contamination by bright stars and extended sources from outside the image boundaries, we identify all the eight images adjacent to each target image, and apply the same masking procedure to those neighboring images. We then merge the external star and galaxy masks that overlap with the target image into the central mask. Finally, we combine the three sets of masks from the gri -bands into a single image mask, so that objects below the detection threshold in one particular band but detected in another would still be masked out in that band. By adopting a single uniform mask across three bands, we also ensure that the measurement of colour profiles is robust against the discrepancy in the masks of different bandpasses.

Figure 1 demonstrates the efficacy of our masking procedure, using the r -band corrected frame of a typical cluster in our sample (with $\lambda=42.6$ and $z=0.233$). Each panel has a dimension of 2248 by 1689 pixels, larger than the original image frame by 200 pixels on each side (i.e., the white strips surrounding each image frame have a width of 100 pixels). Panel (a) shows the false-colour image of the cluster, with the large dashed and small solid concentric circles indicating 1 Mpc and 100 kpc-radius regions centred on the BCG, respectively. Panel (b) is similar to panel (a) but shows the r -band image, with the grayscale indicating the individual pixel

fluxes. Panel (c) shows the masks of the detected stars (cyan solid circles), saturated pixels (black dashed circles), and galaxies (magenta solid ellipses) within the field. The circles within the white strips surrounding the original image frame represent the sources from neighboring parts of the sky. Clearly, some of the bright stars and saturated pixels in the white strips could significantly pollute pixels of the cluster image. Panel (d) shows the final r -band image after all the masks have been applied, including those derived from the g and i -band images. We expect the fluxes within the cluster centre to be dominated by the BCG and ICL, but there still exist some unmasked satellite galaxies, faint background galaxies, and faint foreground stars in the final image of panel (d). We will statistically remove the contamination in the BCG+ICL profiles by the undetected (hence unmasked) background sources in §3.3 and faint satellites in §4.4.

3.2 Image Rescaling to Reference Redshift

To stack images at the same physical scale, we transform all the masked images to the reference redshift $z_{\text{ref}}=0.25$ with the same pixel size. Firstly, we rescale the pixel size of each image by the square of the angular diameter distance ratio between the observed and reference redshifts, $(D_A^{\text{obs}}/D_A^{\text{ref}})^2$, and the flux within the pixel by the square of the ratio between the two luminosity distances, $(D_L^{\text{obs}}/D_L^{\text{ref}})^2$. Cosmic dimming is automatically included as the pixel SB scales with $[(1+z_{\text{obs}})/(1+z_{\text{ref}})]^4$. We do not apply any K -correction to the cluster fluxes due to the lack of robust SED templates for the ICL. However, since the reference redshift is close to the median redshift of the sample, we anticipate that the amount of K -correction in the stacked images should be largely cancelled out. [We explicitly test this using the colours of the BCGs to compute the distribution of \$K\$ -correction values in each band, and find that the mean \$K\$ -corrections are close to zero with a scatter of 0.025](#)

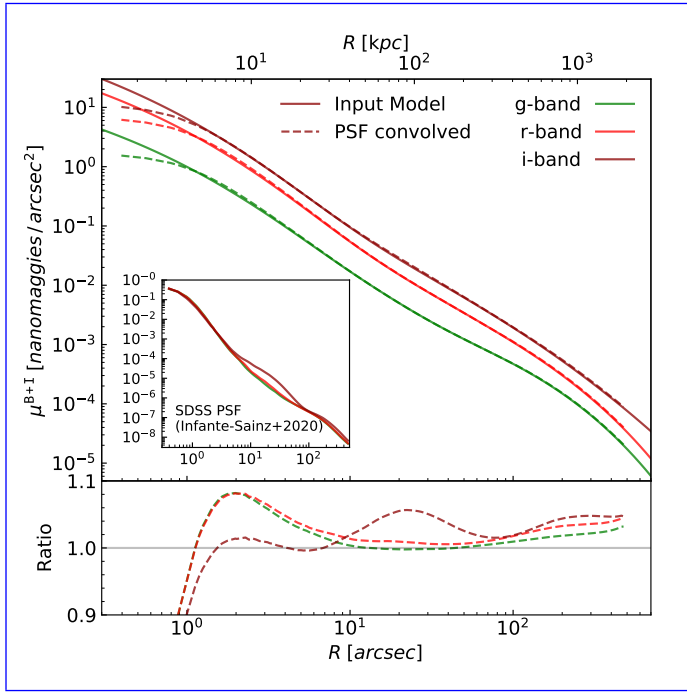


Figure 4. Impact of the SDSS PSF on the BCG+ICL SB profiles. *Top:* Surface brightness profiles in the g (green), r (red), and i-band (maroon). Solid curves are the input three-Sérsic models of the SB profiles before convolving with the PSF, and the dashed curves are the results after convolving them with the PSF derived by Infante-Sainz (2020) in each band (illustrated in the inset panel, where the PSF in each band is normalized to have unit total flux). *Bottom:* The ratio between the SB profiles after and before PSF convolution. The bottom and top x-axes are in units of arc sec and kpc (physical), respectively.

magnitude in the i-band, which contributes to a 1–2% uncertainty in the stellar surface density profiles. In addition, we correct for Galactic extinction on the stacked images using the average A_V of the BCG sightlines, rather than the individual imagesBCGs. Secondly, we resample all the rescaled images to 0.396'' per pixel, i.e., the original pixel size of the SDSS images. We then redistribute the image fluxes into the resampled pixels, so that the flux in pixel i (after resampling) is $f_i = \sum_j \mu_j A_{ij}$, where μ_j is the SB of the j -th pixel in the rescaled image (i.e., before resampling) and A_{ij} is the overlapped area between pixel i and pixel j .

3.3 BCG+ICL SB Profile Measurement

With all clusters shifted to the reference redshift, we now stack their images centred on the BCGs in physical coordinates. We do not rotate the cluster images, e.g., to align the BCGs by their major axes, as we are mainly concerned with the 1D azimuthally-averaged profiles in this paper. We carefully account for the masked regions and adopt the mean flux at each pixel for the stacked image. A total SB profile $\mu^{\text{tot}}(R)$ is then computed as the azimuthally averaged SB within each annulus of radius R . However, this total SB profile includes not only the light from the BCG+ICL, but also contributions from the unmasked satellite galaxies, background galaxies, and foreground stars (i.e., foreground stars, and the Galactic cirrus (which is uncorrelated with the cluster positions on the sky), hence a BCG+ICL+Background \neq SB profile). We will estimate

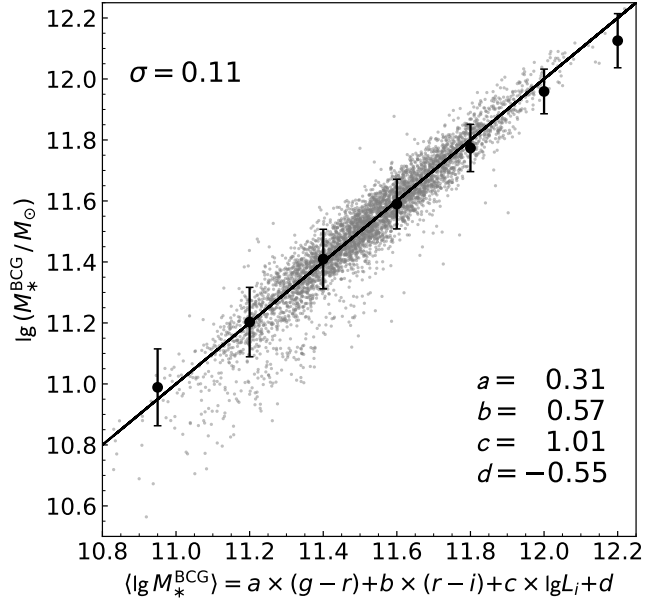


Figure 5. Comparison between the BCG stellar mass M_*^{BCG} measured from template fitting (y-axis) and that predicted by our linear M_*/L_r estimator (x-axis). Black circles with errorbars indicate the median relation with its scatter (~ 0.11 dex), in good agreement with the one-to-one relation (black line). The parameters of the M_*/L_r estimator are listed in the bottom right corner.

the unmasked satellite contribution by inspecting the satellite stellar mass functions later in §4.4, and describe the removal of the background SB induced by the other two-three components below.

For any given set of clusters, we select a matching sample of random clusters with the same joint distribution of redshift and richness from the SDSS redMaPPer random catalogue v6.3. Since the sensitivity of redMaPPer algorithm to the background (e.g., survey boundary, masks, and variation of photometric depth) is incorporated in the generation of random clusters (Rykoff et al. 2016), we expect the background SB of the random cluster images to be similar to that of the observed ones. To measure the background SB profile, we download the SDSS corrected frames that host the random clusters, and perform the same two-step quality inspection to remove defect images from the random sample. We then apply the same masking, rescaling, and stacking procedures to the random cluster images that pass the inspection, thereby producing a background SB profile for the clusters. We repeat such procedure ten times by reshuffling the relative positions of the random BCGs on the images after each measurement, and calculate the average of the ten measurements as our the final background SB profile $\mu^{\text{bkg}}(R)$.

Finally, we derive the BCG+ICL SB profile $\mu^{\text{B+I}}(R)$ by subtracting the background SB profile from the total SB profile,

$$\mu^{\text{B+I}}(R) = \mu^{\text{tot}}(R) - \mu^{\text{bkg}}(R). \quad (1)$$

We further normalise the $\mu^{\text{B+I}}(R)$ profile to be zero at projected distance $R=2$ Mpc, and focus on the SB signals at $R < 1$ Mpc for the rest of the paper. Note that the $\mu^{\text{B+I}}(R)$ profile measured in this way includes the contribution from the faint satellite galaxies that are unmasked. We do not subtract this contribution from our measured $\mu^{\text{B+I}}(R)$ and $\Sigma_*^{\text{B+I}}(R)$ profiles, but will nonetheless estimate the total stellar mass of the unmasked satellites $\Sigma M_*^{\text{unmasked}}$ in §4.4.

In order to estimate the uncertainties of $\mu^{B+I}(R)$, we employ the standard Jackknife resampling technique by dividing each cluster sample into 30 equal-size subsamples, and compute estimate the error matrix from the 30 “leave-one-out” measurements (i.e., using 29 subsamples for each resampled measurement) experiments (Efron & Stein 1981).

Figure 2 shows the stacked 2D image of the BCG+ICL SB distribution (left) and the corresponding 1D SB profiles (right) for our overall cluster sample in the r band. In the left panel, the grayscale intensity represents the SB of each pixel, while the contour lines indicate seven levels of SB ranging from $\mu=26$ mag/arcsec 2 at $R\approx 50$ kpc to 32 mag/arcsec 2 at $R\approx 1$ Mpc (with $\Delta\mu=1$ mag/arcsec 2 increasing outwards), obtained using smoothing kernels of 3, 7, 11, 17, 29, 29, and 29 pixels, respectively and colour-coded by the vertical colourbar on the right. The azimuthally averaged 1D SB profiles are shown in the right panel, where the blue dashed, gray dotted, and red solid curves indicate the total stacked SB $\mu^{tot}(R)$ (BCG+ICL+background), background SB $\mu^{bkg}(R)$, and the BCG+ICL SB profiles $\mu^{B+I}(R)$, respectively. The dot-dashed vertical line indicates the physical scale that the PSF (point spread function) size corresponds to at $z=0.25$ (the same as the dot-dashed vertical lines in both panels of Figure 3). The shaded bands indicate the SB uncertainties estimated from Jackknife resampling. Thanks to the large sample size, we are able to robustly measure the diffuse cluster light down to roughly 32 mag/arcsec 2 at $R=1$ Mpc despite the relatively shallow depth of the SDSS imaging from a decade ago.

We compare our BCG+ICL SB (left) and $g-r$ colour (right) profiles with the results from previous studies in Figure 3. In the left panel, solid and dashed curves indicate the $\mu^{B+I}(R)$ profiles measured for the redMaPPer clusters in this work and the maxBCG (Koester et al. 2007) clusters by Z05, respectively, in the SDSS g (green), r (red), and i (maroon) bands. The amplitudes of the maxBCG profiles are slightly higher than the redMaPPer ones on all scales, likely because the maxBCG clusters selected by Z05 are on average higher mass systems than ours. On small scales, our stacked profiles are consistent with the average BCG light profiles (dotted) derived by the SDSS photometric pipeline (profMean), but the dotted curves are rapidly cut off on scales above 30 kpc. For the $g-r$ color profiles shown in the right panel, our measurement (red solid) is slightly redder than the that of Z05 (black dot-dashed), consistent with the Z05 BCGs being more massive. We also show the DES $g-r$ colour profile measured by Zhang et al. (2019) for the DES clusters (cyan dashed), which exhibits a similar slope compared to Z05 and our results. The Zhang et al. profile is measured from a much smaller cluster sample than ours with ~ 280 DES redMaPPer clusters, so their measurements are cut off at 200 kpc despite the DES photometry is roughly two magnitudes deeper than SDSS.

Note that none of the BCG+ICL SB profile measurements shown in Figure 3 are corrected for the wide-angle effect of the PSF (Tal 2011; D’Souza 2014; Wang 2019). To test the impact of PSF on the diffuse light on large scales, Zhang et al. (2019) fit a model with three Sérsic components to the measured BCG+ICL SB profile, and convolve the best-fitting model curve with the DES PSF in each band. They found that the SB enhancement due to PSF on scales above 100 kpc is smaller than a few percent and is thus negligible in the ICL analysis. Adopting the same approach, we fit a three Sérsic model to the BCG+ICL SB profile in each band, and convolve them with the SDSS PSF model inferred by Infante-Sainz (2020). Figure 4 compares the difference between the SB profiles before (solid) and after (dashed) the PSF convolution in the g (green), r (red), and i (maroon) bands, respectively.

The inset panel illustrates the SDSS PSF model inferred by Infante-Sainz (2020), normalized so that total flux is unity in each band, and the dashed curves in the bottom panel show the ratio profiles between the SB profiles after and before PSF convolution. In the g - and r -bands, the relative difference is well below 2% and 5% on scales between 20 – 400 kpc and above 400 kpc at redshift 0.25, respectively. The difference in the i -band is slight larger due to the bump feature at ~ 20 arcsec in the i -band PSF, but is still below 6% on all scales above 10 kpc and smaller than the statistical uncertainties on scales above 100 kpc. We have also examined the impact of the PSF on all the other measurements in our paper, and find that our conclusions are unaffected by the wide-angle effect of the SDSS PSF.

4 STELLAR SURFACE DENSITY PROFILE

4.1 Mass-to-Light Ratio

For each cluster sample, we now convert the light profiles μ^{B+I} measured in three bands into a BCG+ICL stellar surface density profile Σ_*^{B+I} using an empirically calibrated mass-to-light ratio against the M_{*}^{BCG} measured in §2.1. In particular, we assume the i -band mass-to-light ratio (M_{*}/L_i) can be described by a simple linear function of the i -band luminosity L_i , $g-r$, and $r-i$ colours,

$$\lg(M_{*}/L_i) = a \cdot (g - r) + b \cdot (r - i) + (c - 1) \cdot \lg L_i + d. \quad (2)$$

We use M_{*}^{BCG} , i -band cModel magnitudes, and the model magnitude colours of the BCGs to infer the values of $\{a, b, c, d\}$ via least-square fitting. Figure 5 demonstrates the efficacy of our empirical calibration of M_{*}/L_i , where we show the distribution of BCGs on the observed vs. predicted M_{*}^{BCG} plane. Filled circles with error-bars indicate the mean observed M_{*}^{BCG} at fixed $\langle M_{*}^{BCG} \rangle$ predicted by Equation 2 with $\{a=0.31, b=0.57, c=1.01, d=-0.55\}$, in good agreement with the one-to-one relation (solid line). The outliers in the bottom left corner mainly consist of BCGs with relatively blue colours, which have minimal impact on the least-square fit due to their small fraction.

However, since the outer ICL has a bluer colour than the inner BCG (right panel of Figure 3), extrapolating Equation 2, which is calibrated against the inner BCG, to the outer ICL at $R>200$ kpc may incur a systematic bias in the Σ_*^{B+I} measurement. Fortunately, the bias should be sufficiently small compared to our measurement uncertainties at those radii. For example, a 10% bias in the coefficient a would result in a 0.03 dex bias in stellar mass for $g-r \approx 1$, much smaller than the 20% statistical uncertainty of Σ_*^{B+I} at $R \sim 200$ kpc (as will be described further below). Furthermore, our detection of R_{SOI} relies on the difference between the Σ_*^{B+I} of two cluster subsamples, so the M_{*}/L_i -induced bias in Σ_*^{B+I} should be largely cancelled out.

4.2 Surface Density Profiles of Stars, Dark Matter, and Galaxies

In the left panel of Figure 6, we apply our best-fitting formula of M_{*}/L_i (Equation 2) to the gri SB profiles in Figure 3 and derive the BCG+ICL stellar surface density profile $\Sigma_*^{B+I}(R)$ for the overall cluster sample, as shown by the open circles with errorbars. Clearly, the Σ_*^{B+I} profile has a significant ICL component that extends to a few $\times 10^4 M_{\odot}$ kpc $^{-2}$ at scales ~ 500 kpc–1 Mpc, where we expect that the ICL largely follows the distributions of dark matter and satellite galaxies. To compare the surface density profile of the

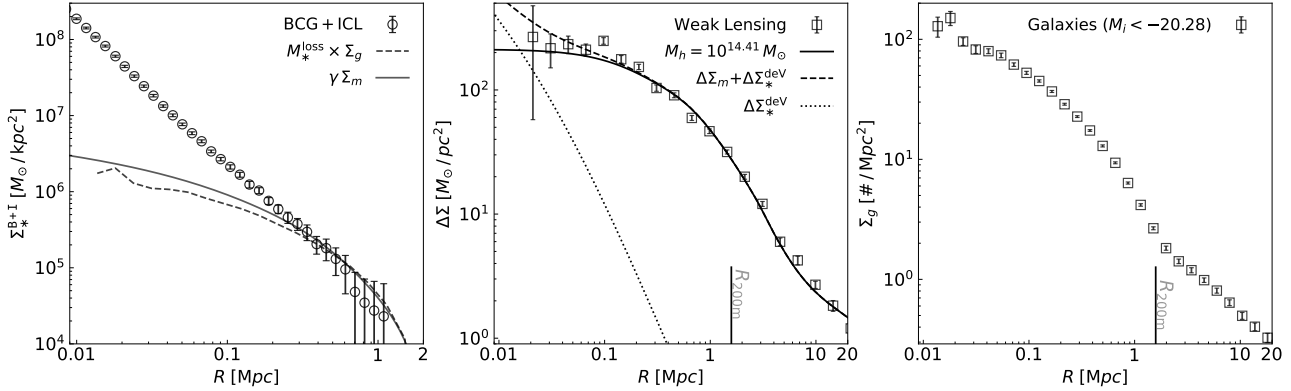


Figure 6. Distribution of stars, dark matter, and galaxies around the BCG. *Left:* Stellar surface mass density profiles. Open circles with errorbars are the $\Sigma_*^{B+I}(R)$ profile measured by this work, while solid ($\gamma\Sigma_m$) and dashed black ($M_*^{\text{loss}}\Sigma_g$) curves are the model predictions assuming that the outer ICL follows the distributions of dark matter (middle panel) and satellite galaxies (right panel), respectively. The best-fitting scaling factors are $\gamma=1/446$ and $M_*^{\text{loss}}=1.4\times10^{10} M_\odot$. *Middle:* Surface density contrast $\Delta\Sigma(R)$ measured by cluster weak lensing (squares with errorbars) and predicted by the best-fitting model described in Z21 (solid). Dotted curve indicates the weak lensing contribution from the stellar mass of the best-fitting de Vaucouleurs' profile, and dashed curve is the sum of the two contributions. *Right:* Galaxy surface number density profile $\Sigma_g(R)$ measured from the cluster-galaxy cross-correlation function. The vertical lines in the middle and right panels mark the halo radius R_{200m} .

diffuse component with that of the dark matter and satellite galaxies, we show the measurements of cluster weak lensing $\Delta\Sigma$ and galaxy number density profile Σ_g for the overall sample in the middle and right panels of Figure 6, respectively (squares with errorbars).

We obtain the $\Delta\Sigma$ and Σ_g measurements (as well as the theoretical model of $\Delta\Sigma$) by faithfully following the methods described in Z21. Briefly, the surface density contrast profile $\Delta\Sigma(R)$ is measured from weak lensing using the DECaLS DR8 imaging (Dey et al. 2019), while the galaxy surface number density profile $\Sigma_g(R)$ is calculated by cross-correlating clusters with the photometric galaxies within SDSS DR8. The photometric galaxies are selected with an effective absolute magnitude limit of $M_i = -20.28$. We also show the best-fitting $\Delta\Sigma_m(R)$ profile predicted by the theoretical model of Z21 in the middle panel (solid curve), which describes the small-scale lensing using an NFW halo density profile (with the cluster miscentring effect constrained by X-ray observations), and the large-scale lensing using a biased version of the matter clustering. From the $\Delta\Sigma$ modelling, we infer the average halo mass of our cluster sample to be $M_h = 2.57 \times 10^{14} M_\odot$, consistent with the results from Z21. The dotted curve indicates the $\Delta\Sigma^{deV}$ signal from the stellar mass of the best-fitting de Vaucouleurs' profile at $R < 20$ kpc, and the dashed curve shows the sum of $\Delta\Sigma^{deV}$ and $\Delta\Sigma_m$. The vertical lines in the two panels indicate the halo radius R_{200m} inferred from the weak lensing mass. The $\Sigma_g(R)$ profile exhibits an inflection at R_{200m} , indicating the familiar transition from the 1-halo term (dominated by satellite galaxies) to the 2-halo term in the halo occupation distribution language (e.g., Zu & Mandelbaum 2015). We refer interested readers to Z21 for technical details that are beyond the scope of this paper.

Returning to the left panel of Figure 6. Solid and dashed curves show the matter surface density profile Σ_m and galaxy surface number density profile Σ_g , multiplied by a scale factor γ and the average mass loss per galaxy M_*^{loss} , respectively. In particular, Σ_m is related to $\Delta\Sigma$ via

$$\Delta\Sigma(R) = \overline{\Sigma_m}(<R) - \Sigma_m(R), \quad (3)$$

where $\overline{\Sigma_m}(<R)$ is the average surface mass density within R . The

scaling factor is defined as

$$\gamma(R) = \frac{\Sigma_{\text{ICL}}(R) + \Sigma_{\text{sat}}^{\text{unmasked}}(R)}{\Sigma_m(R)} \quad (4)$$

where Σ_{ICL} is the ICL stellar mass profile and $\Sigma_{\text{sat}}^{\text{unmasked}}$ is the stellar mass profile of the unmasked satellite galaxies. By assuming that the ICL and unmasked satellites both follow the distribution of dark matter, the above equation can be simplified as

$$\gamma(R) \equiv \gamma = f_{\text{ICL}} + f_{\text{sat}}^{\text{unmasked}}, \quad (5)$$

where f_{ICL} and $f_{\text{sat}}^{\text{unmasked}}$ are the ICL and unmasked satellite stellar-to-halo mass fractions, respectively. We infer the best-fitting values of $\gamma=1/446$ and $M_*^{\text{loss}}=1.4\times10^{10} M_\odot$ by matching the scaled profiles to the $\Sigma_*^{B+I}(R)$ measurements above $R=400$ kpc. We will infer the values of f_{ICL} and $f_{\text{sat}}^{\text{unmasked}}$ separately in §4.4. Note that we predict the Σ_m profile from the best-fitting $\Delta\Sigma$ model curve in the middle panel, and directly adopt the observed Σ_g profile in the right panel. Additionally, both curves are normalized to have zero amplitudes at $R=2$ Mpc, following the same practice when measuring Σ_*^{B+I} .

Overall, the two scaled profiles $\gamma\Sigma_m$ and $M_*^{\text{loss}}\Sigma_g$ in the left panel of Figure 6 provide good descriptions to the BCG+ICL stellar surface density profiles at $R>400$ kpc, indicating that the ICL in the outer region of clusters indeed follows the distribution of the dark matter and satellite galaxies. This is consistent with the findings from Montes & Trujillo (2019), which suggested that the ICL is an excellent tracer of dark matter, as well as satellite stripping being the dominant channel of ICL production in the outer region. In particular, we find that our observation of the diffuse light on scales above 400 kpc can be explained if $\sim 0.1\text{--}0.2\%$ of the total mass is in the form of ICL, and if $\sim 10^{10} M_\odot$ of stars were stripped from each satellite galaxy into the ICL.

4.3 Decomposition of the BCG+ICL Surface Stellar Mass Profile

Given that the outer region of the ICL roughly follows the distribution of dark matter, we can separate the observed BCG+ICL stellar surface mass profile Σ_*^{B+I} into at least two physically distinct

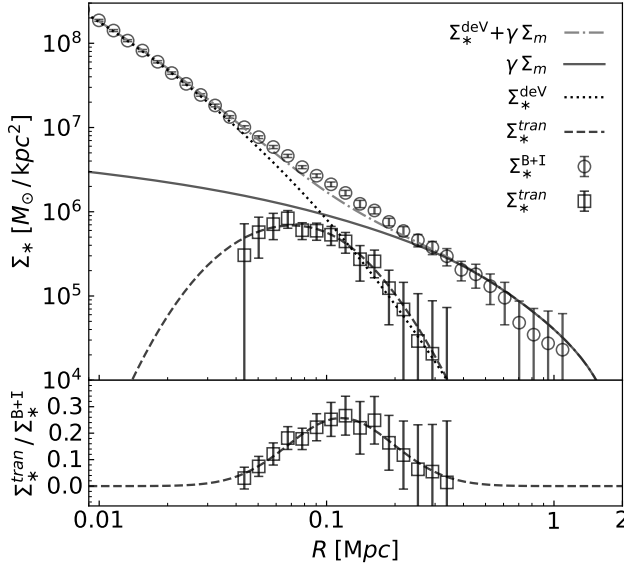


Figure 7. Decomposition of the BCG+ICL stellar surface mass density profile $\Sigma_*^{B+I}(R)$ (open circles with errorbars). Solid curve is the total surface mass density profile Σ_m , scaled by $\gamma=1/446$ (Equation 4), while the best-fitting de Vaucouleurs profile for the Σ_*^{B+I} profile at $R<20$ kpc is shown as the dotted curve. The sum of $\gamma\Sigma_m$ and Σ_*^{dev} is indicated by the dot-dashed curve, revealing an excess mass in the observed Σ_*^{B+I} profile on transitional scales of $R\sim70-200$ kpc. Open squares with errorbars indicate this transitional component Σ_*^{tran} . The bottom subpanel shows the ratio between $\Sigma_*^{tran}(R)$ and $\Sigma_*^{B+I}(R)$, which can be described by a simple Gaussian (dashed; Equation 9).

components, including one that follows the dark matter on large scales ($R=400$ kpc–1Mpc) and the other BCG-dominated portion on small scales ($R<50$ kpc). By further assuming that the *intrinsic* BCG can be described by a de Vaucouleurs’ profile, the BCG-dominated portion may include a third component on transitional scales where the extended BCG envelope unfolds into the ICL. Following this philosophy, we can decompose the Σ_*^{B+I} profile via the following three steps. Firstly, we adopt the total surface mass profile Σ_m inferred from weak lensing, and multiply it by $\gamma=1/446$ to describe Σ_*^{B+I} at $R>400$ kpc, as was done in the left panel of Figure 6.

$$\gamma\Sigma_m(R) = \Sigma_*^{ICL}(R) + \Sigma_*^{unmasked}(R) \quad (6)$$

Secondly, we fit a de Vaucouleurs’ profile to the Σ_*^{B+I} measurement on scales below $R=20$ kpc,

$$\Sigma_*^{dev}(R) = \Sigma_e \exp \left(-7.676 \left[(R/R_e)^{1/4} - 1 \right] \right), \quad (7)$$

yielding $\Sigma_e=10^{7.93} M_\odot/\text{kpc}^2$ and $R_e=15.06$ kpc. Finally, we subtract $\gamma\Sigma_m$ and Σ_*^{dev} from the measured Σ_*^{B+I} profile, leaving us a “transitional component”

$$\Sigma_*^{tran}(R) = \Sigma_*^{BCG+ICL}(R) - \left[\Sigma_*^{dev}(R) + \gamma\Sigma_m(R) \right]. \quad (8)$$

Therefore, $\Sigma_*^{tran}(R)$ represents the excess component in the diffuse light that cannot be described by the sum of a de Vaucouleurs’ profile and an ICL mass profile that follows the dark matter.

Figure 7 illustrates the physical decomposition of our observed Σ_*^{B+I} profile (open circles with errorbars) into three distinct components: a de Vaucouleurs’ profile Σ_*^{dev} (dotted curve), a scaled

dark matter profile $\gamma\Sigma_m$ (solid curve), and a transitional component Σ_*^{tran} (open squares with errorbars). The errorbars of Σ_*^{tran} are inherited from that of the Σ_*^{B+I} measurement, assuming zero uncertainties from the subtraction. Additionally, dot-dashed curve indicates the sum of the de Vaucouleurs’ profile and the scaled dark matter profile, which clearly under-predicts the signal on scales between 50 kpc and 300 kpc — a third component Σ_*^{tran} is required to fully describe the diffuse light. The ratio profile between $\Sigma_*^{tran}(R)$ and $\Sigma_*^{B+I}(R)$ is shown in the bottom panel of Figure 7. The transitional component accounts for about 17% of the total diffuse mass on scales between 50 kpc and 300 kpc, and the ratio peaks at 25% around 100 kpc.

To test the robustness of $\Sigma_*^{tran}(R)$, we fit the de Vaucouleurs’ profile to a larger maximum radius of 30 kpc, finding that the centroid and amplitude of $\Sigma_*^{tran}(R)$ stay almost unchanged. We also perform the decomposition using a generic Sérsic profile instead of a de Vaucouleurs’ profile, which has a fixed Sérsic index of four. Although the peak amplitude reduces from 25% to 15% once we allow the Sérsic index to deviate from four, the centroid stays unchanged at ~ 100 kpc and the $\Sigma_*^{tran}(R)$ component remains significant compared to the Σ_*^{B+I} uncertainties ($\sim 5\%$ at $R=100$ kpc). Therefore, we conclude that the transitional component is required to provide a complete description of the diffuse stellar mass profile on scales between 50 kpc and 300 kpc, regardless of assumptions for the stellar mass profile of the inner BCG. For the rest of the paper, we will adopt the $\Sigma_*^{tran}(R)$ profile calculated from assuming a de Vaucouleurs’ profile at $R<20$ kpc as our fiducial model of the transitional component.

Finally, the ratio profile between Σ_*^{tran} and Σ_*^{B+I} (shown in the bottom panel of Figure 7) can be described by a Gaussian (in log-space):

$$\frac{\Sigma_*^{tran}(R)}{\Sigma_*^{B+I}(R)} = f_t \exp \left[-\frac{(\lg R - \lg R_t)^2}{2\sigma_t^2} \right], \quad (9)$$

where $f_t=0.26$, $\sigma_t=0.23$ dex, and $R_t=116.0$ kpc are the amplitude, characteristic log-width, and centroid of the transitional component, respectively. The best-fitting function is shown as the dashed curves in both panels of Figure 7.

4.4 Stellar Mass Budget of Clusters

With the physical decomposition in Figure 7, we are now ready to derive the stellar mass budget of clusters in three states: BCG (i.e., de Vaucouleurs + transitional), ICL, and satellite galaxies. In order to estimate the total amount of stellar mass inside the satellite galaxies, we make use of the conditional stellar mass function (CSMF) of clusters inferred by Yang et al. (2012). In particular, we adopt the shape of the measured CSMF for their halo mass bin of $10^{14.2}-10^{14.5} h^{-2} M_\odot$ (c.f., column 9, table 7 of Yang et al. 2012), which can be described by a Schechter function

$$\frac{dN(M_*/M_h)}{d \lg M_*} = \Phi^\star \left(\frac{M_*}{M^\star} \right)^{\alpha+1} \exp \left(-\frac{M_*}{M^\star} \right) \quad (10)$$

with $M^\star=8.32 \times 10^{10} M_\odot$ and $\alpha=-1.093$. However, the Yang et al. CSMF was measured for a sample of galaxy groups at $z<0.1$, which has a different value of Φ^\star than that of our cluster sample at $z\sim 0.25$. To determine Φ^\star , we obtain the number of satellite galaxies above our i -band absolute magnitude limit of -20.28 to be 60 per halo, by integrating the galaxy surface number density profile Σ_g to $r_{200m}=1.58$ Mpc (right panel of Figure 6). Given that the i -band

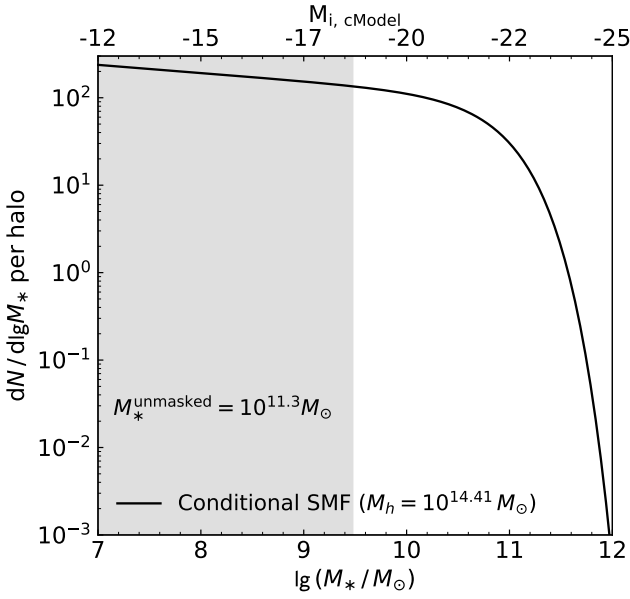


Figure 8. Conditional satellite stellar mass function of our cluster sample (solid curve). Gray shaded region indicates the stellar mass range of satellites that are undetected by our source finding algorithm (hence unmasked). The top x-axis shows the corresponding *i*-band cModel absolute magnitudes (assuming at the reference redshift 0.25). The total stellar mass of the unmasked satellite galaxies is $M_*^{\text{unmasked}} = 2 \times 10^{11} M_\odot$.

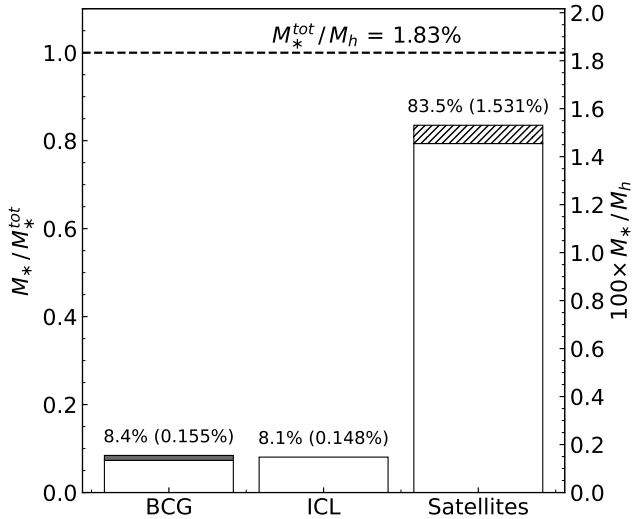


Figure 9. Stellar mass budget of our cluster sample in BCG, ICL, and satellites. Gray filled and hatched portions indicate the contributions from the transitional component and the unmasked satellite galaxies, respectively. The stellar mass fraction (left y-axis) and stellar-to-halo mass fraction (right y-axis) of each component are marked by the percentage values out and inside the parentheses, respectively. The horizontal line indicates the total stellar-to-halo mass fraction of the clusters M^{tot}_*/M_h .

magnitude of -20.28 roughly corresponds to $\lg M_* = 10.2$ (assuming a M_*/L_i of 1.88), we normalise Equation 10 for our cluster sample by enforcing the total number of satellites above $\lg M_* = 10.2$ to be 60 per halo, yielding a $\phi^* = 79.8$ galaxies per dex in M_* per halo. Figure 8 shows the correctly normalized CSMF of our cluster sample (solid curve), which we integrate across the entire stellar mass range to obtain the average stellar mass of the satellites $\langle M_*^{\text{sat}} \rangle = 1.34 \times 10^9 M_\odot$ and the total amount of satellite stellar mass $\Sigma M_*^{\text{sat}} = 3.94 \times 10^{12} M_\odot$.

Furthermore, the gray shaded region (below $\lg M_* = 9.48$) in Figure 8 indicates the stellar mass range that is below the detection threshold of our source finding algorithm, hence unmasked during the SB measurement. This detection threshold roughly corresponds to the *i*-band limiting cModel magnitude of 22.08, i.e., an absolute magnitude of -18.49 for a galaxy at $z \sim 0.25$, yielding a total unmasked stellar mass of $M_*^{\text{unmasked}} = 2 \times 10^{11} M_\odot$. We remove this unmasked stellar mass contribution from the ICL stellar mass budget as follows. The unmasked satellite mass fraction is $f_{\text{sat}}^{\text{unmasked}} = \Sigma M_*^{\text{unmasked}} / M_h = 0.0762\%$. Since the scale factor defined in Equation 5 is $\gamma = 1/446$, the ICL mass fraction is $f_{\text{ICL}} = \gamma - f_{\text{sat}}^{\text{unmasked}} \approx 1/675$.

Finally, Figure 9 shows the stellar mass budget of our cluster sample. We show the stellar mass fractions of the BCG, ICL, and satellites in the left y-axis, and the stellar-to-halo mass fractions of the three components in the right y-axis. The gray filled portion on top of the ‘‘BCG’’ histogram indicates the integrated mass within the Σ_*^{tran} profile ($5.3 \times 10^{10} M_\odot$) shown in Figure 7, while the hatched region on top of the ‘‘Satellites’’ histogram corresponds to the total stellar mass of the unmasked satellites in Figure 8. The dashed horizontal line in the top indicates the total stellar mass-to-halo mass fraction (1.83%) assuming a halo mass of $2.57 \times 10^{14} M_\odot$ measured from weak lensing in Z21. Assuming further that the total baryon fraction of the clusters is the cosmic value $f_b = \Omega_b / \Omega_m \approx 16\%$, we can infer that $\sim 88\%$ of the baryons are in the form of hot gas within clusters. For the stellar mass budget, 83.5% of the stellar mass is inside the satellite galaxies and 8.4% is in the BCG, leaving 8.1% of the stellar mass in the diffuse form of free-floating ICL stars—hence stellar-to-halo mass ratios of 1.531% (satellites), 0.155% (BCG), and 0.148% (ICL). Using the DES imaging, Zhang et al. (2019) estimated that the luminosity fraction of BCG+ICL is $44 \pm 17\%$, but they did not subtract the contribution from undetected satellites. In our stellar mass budget, the sum of the stellar fraction of the BCG+ICL and undetected satellites is about 21%, comparable to the lower end of the Zhang et al. (2019) estimation.

5 BCG SPHERE OF INFLUENCE: DETECTING R_{SOI}

Although we tentatively assign the transitional component to the BCG in Figure 9, it is unclear whether this stellar mass excess is primarily tied to the BCG or the richness. Despite accounting only for $\sim 1\%$ of the total stellar mass, this transitional component is key to solving the sphere of influence of the BCGs R_{SOI} . In particular, if the excess mass is primarily richness-induced, we expect R_{SOI} to stop at $R_t \times 10^{-\sigma_t} \approx 70$ kpc; but a BCG-induced origin would extend R_{SOI} beyond the transitional component at $R_t \times 10^{\sigma_t} \approx 200$ kpc. In this section, we divide our overall cluster sample into two subsamples of different average BCG stellar mass M_*^{BCG} at fixed satellite richness λ , and aim to distinguish the two physical scenarios by comparing the two sets of diffuse light and mass profiles.

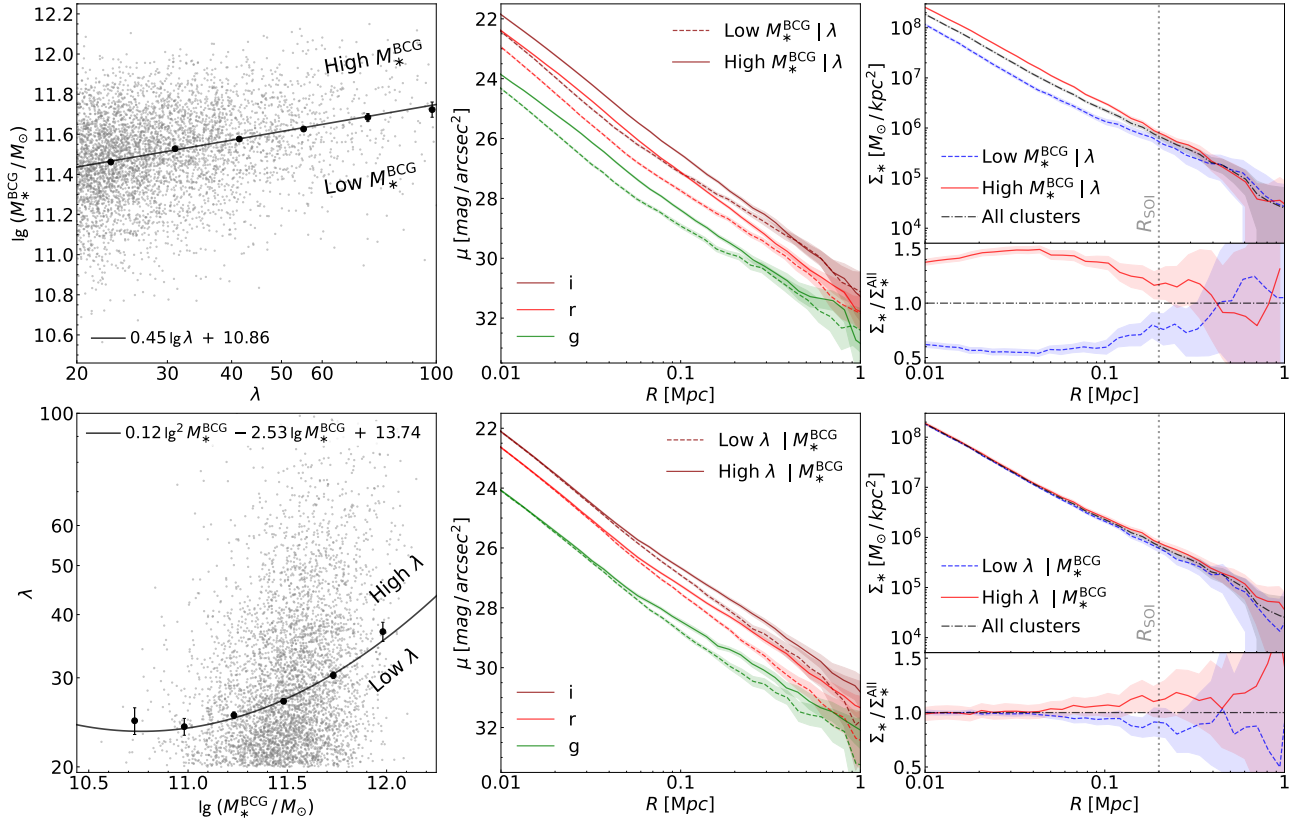


Figure 10. Distributions of clusters on the λ vs. M_*^{BCG} plane (left), surface brightness profiles (middle), and stellar surface density profiles (right) of cluster subsamples split by M_*^{BCG} (top row) and λ (bottom row). *Top left:* Circles show the median of $\lg M_*^{\text{BCG}}$ at fixed $\lg \lambda$, and black solid line is a linear fit to median relation, which divides the clusters into low and high- M_*^{BCG} subsamples. *Top middle:* Surface brightness profiles $\mu^{\text{B+I}}$ of the low (dashed curves) and high (solid curves) M_*^{BCG} subsamples. Green, red, and maroon curves indicate the measurements from g , r , and i -band images, respectively. *Top right:* Stellar surface density profiles $\Sigma_*^{\text{B+I}}$ of the low- M_*^{BCG} (blue dashed), high- M_*^{BCG} (red solid), and all (gray dot-dashed) clusters. The bottom subpanel shows the ratios of the $\Sigma_*^{\text{B+I}}$ profiles of the low (blue dashed) and high (red solid) M_*^{BCG} subsamples over that of the overall sample. Dotted vertical line indicates $R_{\text{SOI}}=200$ kpc. The panels in the bottom row are similar to those in the top, but for subsamples split by λ at fixed M_*^{BCG} .

5.1 Cluster Subsamples Split by M_*^{BCG}

Following Z21, we split the clusters into two subsamples using the median $M_*^{\text{BCG}}|\lambda$ relation, illustrated by the top left panel in Figure 10. In particular, the median $M_*^{\text{BCG}}|\lambda$ relation (solid line) can be described by

$$\langle \lg M_*^{\text{BCG}} \rangle = 0.45 \lg \lambda + 10.86, \quad (11)$$

dividing the clusters into two halves with the same distribution of satellite richness λ , which we refer to simply as the “high- M_*^{BCG} ” and “low- M_*^{BCG} ” subsamples for the rest of the paper. By applying the methods described in §3 and §4, we measure the BCG+ICL surface brightness profile $\mu^{\text{B+I}}$ (top middle panel) and stellar surface mass profile $\Sigma_*^{\text{B+I}}$ (top right panel) for each of the two subsamples.

In the top middle panel of Figure 10, solid and dashed curves indicate the $\mu^{\text{B+I}}(R)$ profiles of the high and low- M_*^{BCG} subsamples, respectively, in the SDSS g (green), r (red), and i (maroon) bands. By construction, the $\mu^{\text{B+I}}(R)$ profile of the high- M_*^{BCG} subsample is ~ 0.73 magnitudes (in the r and i bands; ~ 0.65 magnitudes in the g band) brighter than that of the low- M_*^{BCG} one on scales well below the effective cModel aperture, i.e., $R_* = 50$ kpc, because the average M_*^{BCG} of the two subsamples differ by ~ 0.34 dex. However, the small-scale discrepancy between the two subsamples persist on scales much larger than R_* , and the two sets of $\mu^{\text{B+I}}$ profiles do not converge within the uncertainties until $R \sim 300$ kpc. Likewise,

the two $\Sigma_*^{\text{B+I}}$ profiles in the top right panel exhibit a significant discrepancy on scales as large as $R \sim 200$ –300 kpc, beyond which they start to converge to the same level of stellar surface mass density.

The comparison between the two $\Sigma_*^{\text{B+I}}$ profiles is better illustrated in the bottom of the top right panel of Figure 10, where we show the $\Sigma_*^{\text{B+I}}$ ratios of the high (red solid) and low (blue dashed) M_*^{BCG} subsamples over the overall sample. The discrepancy between the two ratio profiles is more than a factor of two across all scales below $R = 100$ kpc and declines slowly on larger scales, but still strongly persists at $> 50\%$ level at $R \sim 200$ –300 kpc. Not until distances exceed $R \sim 300$ kpc do the two ratio profiles begin to converge to unity (albeit with large errorbars).

Such discrepancy observed between the two subsamples provides a clear detection of the BCG sphere of influence. Since the two subsamples of clusters have the same richness and differ solely in their BCG stellar mass, the clear transition from the constant discrepancy below $R = 100$ kpc to the apparent convergence above 300 kpc in the top right panel of Figure 10 demonstrates that the BCG sphere of influence extends to scales around $R_{\text{SOI}} \simeq 200$ kpc. Interestingly, such transition at R_{SOI} coincides with the radial extent of the transitional stellar mass component revealed by the $\Sigma_*^{\text{B+I}}$ decomposition in §4.3, i.e., $R_{\text{SOI}} \simeq R_t \times 10^{\sigma_t}$, suggesting a common origin of the two observed “transitions”. In particular, the excess

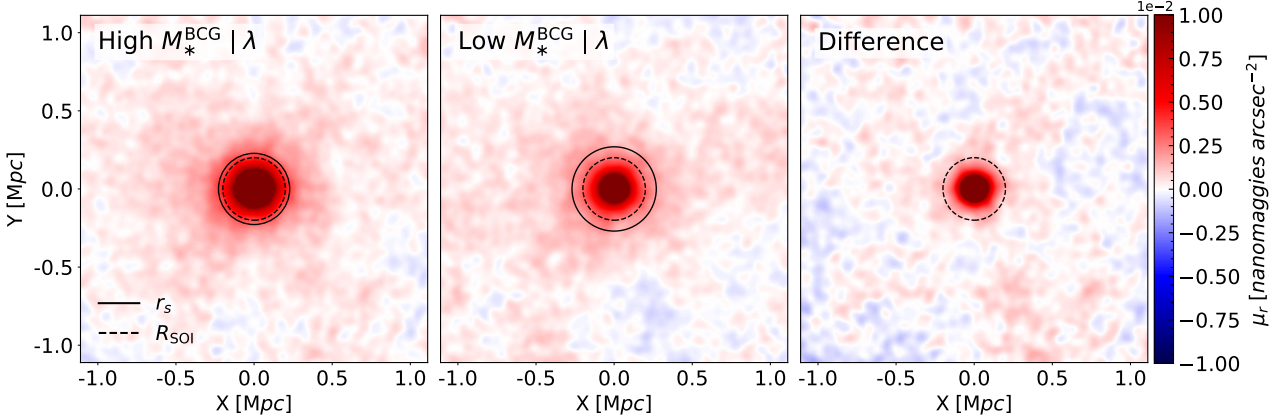


Figure 11. *Left:* Stacked 2D image of the high- M_*^{BCG} clusters, with the pixel SB colour-coded by the vertical colourbar on the right. Solid and dashed circles indicate the cluster characteristic radius ($r_s=227.8$ kpc) and BC G sphere of influence ($R_{\text{SOI}}=200$ kpc), respectively. *Middle:* Similar to the left panel, but for the low- M_*^{BCG} clusters with $r_s=269.7$ kpc. *Right:* The difference image between the high and low- M_*^{BCG} clusters. Clearly, the region outside R_{SOI} (dashed circle) is largely consistent with zero. A smoothing kernel of 15 pixels is applied to the three images.

diffuse light on scales between R_* and R_{SOI} could be primarily formed via processes that simultaneously enriched the BC G, likely due to the tidal disruption/stripping of satellites during periapsis and the violent relaxation after major mergers between the BC Gs and satellites. Furthermore, the convergence of the two $\Sigma_*^{\text{B+I}}$ profiles on scales above 300 kpc confirms our expectation that the ICL in the outer region of clusters largely follows the distribution of satellite galaxies, hence that of the dark matter.

The bottom panels of Figure 10 shows the results of a similar experiment as in the top panels, but by dividing the clusters into low and high- λ subsamples by λ at fixed M_*^{BCG} (bottom left panel). As expected, the two sets of $\mu^{\text{B+I}}$ and $\Sigma_*^{\text{B+I}}$ profiles are consistent on scales below $R_*=50$ kpc, the aperture of our M_*^{BCG} measurements. The two subsamples start to differ on scales above R_* , exhibiting a 20% discrepancy on scales below 100 kpc, much weaker than the factor of two discrepancy between the two M_*^{BCG} splits. The two $\Sigma_*^{\text{B+I}}$ profiles do not reach a discrepancy comparable to that exhibited by the M_*^{BCG} splits until 200 kpc at 50%. This suggests that the diffuse light at 200 kpc has equal contributions from the BC G vs. satellites, further corroborating our conclusion that the BC G sphere of influence ends at $R_{\text{SOI}} \approx 200$ kpc. On scales between R_* and R_{SOI} , the discrepancy between the low and high- λ clusters is significantly smaller than that between the two M_*^{BCG} -split halves, indicating that the influence of satellite richness is subdominant compared to the BC G on those transitional scales — they are firmly within the sphere of influence of the BC G.

Figure 11 provides a more visually-appealing way of comparing the diffuse light distributions between the low and high- M_*^{BCG} subsamples. In particular, we compare the 2D stacked r -band images of the high- M_*^{BCG} (left) and low- M_*^{BCG} (middle) subsamples, with the difference image between the two shown in the right panel. The SB values, in the unit of nanomaggies per arcsec^2 , are computed with a smoothing kernel of 15 pixels, indicated by the colourbar on the right. Solid circles in the left and middle panels indicate the characteristic radii r_s of the high ($r_s=227.8$ kpc) and low ($r_s=269.7$ kpc) M_*^{BCG} clusters, respectively, inferred from weak lensing modelling by Z21. Dashed circle in each panel indicates the BC G sphere of influence with $R_{\text{SOI}}=200$ kpc. Consistent with 1D profiles in the top panels of Figure 10, the high- M_*^{BCG} clusters exhibits a more en-

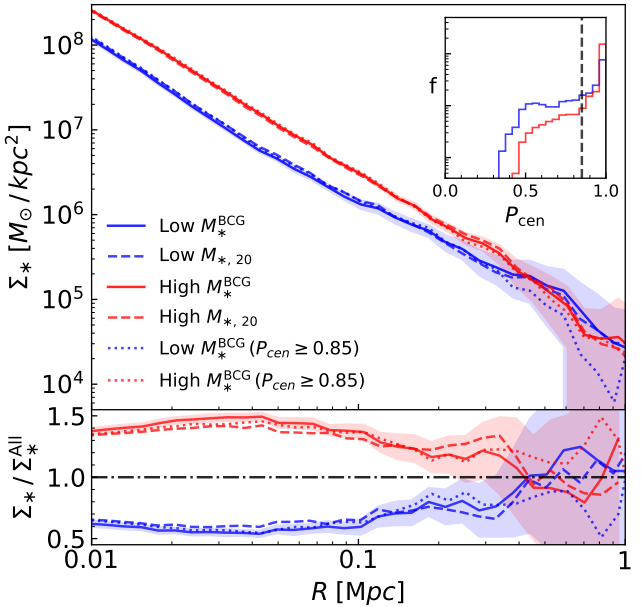


Figure 12. Similar to the top right panel of Figure 10, but with measurements for cluster subsamples split by $M_{*,20\text{kpc}}$ (stellar mass measured within a 20 kpc-aperture; dashed curves) and for clusters with the BC G centring probability $p_{\text{cen}}>0.85$ (dotted curves). Inset panel shows the p_{cen} distributions of the low (blue histograms) and high (red histograms) M_*^{BCG} subsamples, with the vertical dashed line indicating our $p_{\text{cen}}=0.85$ cut.

hanced surface brightness distribution than the low- M_*^{BCG} systems on scales below $\sim R_{\text{SOI}}$, but the two images are almost indistinguishable on scales above ~ 300 kpc — the difference image is consistent with having zero SB at $R>300$ kpc.

5.2 Systematic Tests Against Stellar Mass Aperture and BC G Centering Probability

The key conclusion of our paper, that the BC G sphere of influence extends to a characteristic radius of $R_{\text{SOI}} \approx 200$ kpc, is based on the

experiment of §5.1. However, the experiment could be affected by systematic uncertainties associated with the aperture of our stellar mass estimates or the miscentring effect in the redMaPPer cluster finding algorithm (Johnston et al. 2007; Oguri & Takada 2011; Rozo & Rykoff 2014; Hollowood et al. 2019). For example, although the effective aperture of M_*^{BCG} is $R_* \approx 50$ kpc, the individual apertures of some of the nearby, bright systems could be larger, thereby artificially pushing the discrepancy between the $\Sigma_*^{\text{B+I}}$ of high and low- M_*^{BCG} subsample to larger radii. For miscentring, the average centring probability p_{cen} of the low- M_*^{BCG} clusters is lower (e.g., due to projection effects; see Zu et al. 2017), and is thus more likely to have satellite galaxies misidentified as centrals than their high- M_*^{BCG} counterparts. Consequently, it is plausible that the $\Sigma_*^{\text{B+I}}$ of the low- M_*^{BCG} subsample is heavily underestimated on small scales due to the lack of extended stellar envelope surrounding those misidentified centrals.

To investigate the impact of different stellar mass apertures, we repeat the experiment of §5.1 by adopting $M_{*,20\text{kpc}}$, the stellar mass measured within a fixed aperture of 20 kpc. By splitting the clusters into two subsamples of different $M_{*,20\text{kpc}}$ at fixed λ , we eliminate the possibility that the high- M_*^{BCG} subsample may preferentially select the more extended BCGs. The result of this test is shown as the red (high- $M_{*,20\text{kpc}}$) and blue (low- $M_{*,20\text{kpc}}$) dashed curves in Figure 12. The $\Sigma_*^{\text{B+I}}$ of the high- $M_{*,20\text{kpc}}$ subsample is $\sim 3\%$ lower than that of the high- M_*^{BCG} clusters on scales below 200 kpc, and vice versa for the low- $M_{*,20\text{kpc}}$ subsample. Overall, the discrepancy between the $\Sigma_*^{\text{B+I}}$ profiles of the two subsamples split by $M_{*,20\text{kpc}}$ is very similar to our fiducial measurement split by M_*^{BCG} (solid curves), consistent with the BCG sphere of influence extending to $R_{\text{SOI}} \approx 200$ kpc.

To test the miscentring effect, we measure the p_{cen} distributions of the BCGs of the high (red histograms) and low (blue histograms) M_*^{BCG} subsamples in the inset panel of Figure 12. Both p_{cen} distributions peak at p_{cen} close to 100%, but the distribution of the low- M_*^{BCG} clusters indeed exhibits a longer low- p_{cen} tail. To eliminate the impact of low- p_{cen} systems on our R_{SOI} measurement, we remove clusters with the p_{cen} of their BCGs lower than 85%, shown as the vertical dashed line in the inset panel, and repeat the experiment using the M_*^{BCG} -split subsamples. The results of the miscentring test are shown by the red and blue dotted curves for the high and low- M_*^{BCG} clusters with BCG $p_{\text{cen}} > 85\%$, respectively. Again, we do not find any significant deviation from our fiducial measurements due to the exclusion of the low- p_{cen} systems. Therefore, based on the two systematic tests shown in Figure 12, we conclude that the detection of $R_{\text{SOI}} \approx 200$ kpc is robust against the aperture size of the BCG stellar mass estimates and the level of miscentring in the SDSS redMaPPer catalogue.

5.3 Connection between BCG Sphere of Influence and Halo Concentration

As mentioned in the Introduction, Z21 modelled the weak lensing measurements of the two subsamples split by M_*^{BCG} at fixed λ , and found that the two have the same average halo mass, but the average halo concentration of the high- M_*^{BCG} clusters is $\sim 10\%$ higher than that of the low- M_*^{BCG} systems (for a thorough explanation of such observation, see ?Zu et al. (2022)). Z21 speculated that the strong correlation between halo concentration and M_*^{BCG} could be induced at the early phase of halo growth, when the fast accretion and frequent mergers not only built the characteristic central regions of the cluster haloes, but also fuel the *in situ* stellar growth of the

BCGs. Interestingly, the characteristic radii r_s inferred by Z21 are ~ 200 – 300 kpc, in good agreement with our constraint of R_{SOI} in this paper.

Such similarity between the values of r_s and R_{SOI} is likely physical. In the vicinity of the BCGs, stars could be tidally disrupted/stripped from satellites after periapsis passage or ejected after BCG-satellite major mergers. Most of those stray stars cannot escape to larger radii due to the relatively high escape velocities within r_s . Therefore, a fraction of them would fall back onto the BCGs and grow M_*^{BCG} , while the rest stays unbound to the BCGs and form the transitional component Σ_*^{tran} , which is however well confined within r_s , hence the BCG sphere of influence R_{SOI} . In this scenario, the BCG sphere of influence is primarily shaped by the growth of the BCG, but helped maintained by the concentration of the dark matter halo. Therefore, we expect that R_{SOI} increases with the growth of M_*^{BCG} , but should always stay within the characteristic radius of the halo r_s .

We present a comprehensive comparison between the low (blue squares) and high (red circles) M_*^{BCG} subsamples in their BCG+ICL stellar surface density profiles $\Sigma_*^{\text{B+I}}$ (left), weak lensing profiles $\Delta\Sigma$ (middle), and galaxy surface number density profile Σ_g (right) in Figure 13. The left panel is similar to Figure 7, but with our decomposition method applied to the two subsamples separately. Since we adopt the same $\gamma=1/446$ as for the overall sample, the discrepancy in the total surface matter density profiles $\gamma\Sigma_m$ between the two subsamples below 200 kpc is entirely due to the different halo concentrations. After subtracting the inner de Vaucouleurs' profile and the outer scaled matter surface density profile from each $\mu^{\text{B+I}}$ profile, the transitional component $\Sigma_*^{\text{tran}}(R)$ emerges as the filled symbols with errorbars that we fit using Equation 9 (dashed curves).

Focusing on the $\Sigma_*^{\text{tran}}(R)$ profiles in the left panel of Figure 7, we detect a shift of 26 kpc in the centroid from the low- M_*^{BCG} subsample ($R_t=92$ kpc) to the high- M_*^{BCG} subsample ($R_t=118$ kpc), while the two log-widths are comparable ($\sigma_t=0.22$ and 0.25 dex for low and high- M_*^{BCG} subsamples, respectively). Assuming $R_{\text{SOI}} \approx R_t \times 10^{\sigma_t}$, R_{SOI} increases with M_*^{BCG} from $R_{\text{SOI}}^{\text{low}}=153$ kpc to $R_{\text{SOI}}^{\text{high}}=210$ kpc. Moreover, the integrated mass within the transitional component Σ_*^{tran} of the high- M_*^{BCG} subsample is $8.56 \times 10^{10} M_\odot$ ($f_t=0.29$), about 0.48 dex higher than that of the low- M_*^{BCG} subsample with $2.81 \times 10^{10} M_\odot$ ($f_t=0.24$) — slightly larger than the 0.34 dex difference between average M_*^{BCG} .

The middle panel of Figure 13 is similar to the Figure 5 of Z21, showing the weak lensing comparison between the two subsamples. We include the weak lensing signals predicted on small scales by the de Vaucouleurs' profiles of the BCGs (dotted curves) in the prediction of the total $\Delta\Sigma$ (dashed curves). The 10% difference in halo concentration is manifested by the discrepancy between the two $\Delta\Sigma$ profiles on scales between 100 kpc and 500 kpc, which then translates to the discrepancy in their total surface matter density profiles Σ_m below 200 kpc in the left panel. We compare the two galaxy surface number density profiles in the right panels of Figure 13 (similar to the right panel of Figure 6 in Z21). Clearly, the galaxy distributions around the BCGs of the two subsamples are almost indistinguishable, further corroborating our conclusion that the differences in $\Sigma_*^{\text{B+I}}$ (left) and $\Delta\Sigma$ (middle) are tied solely to the discrepancy in M_*^{BCG} and/or halo concentration.

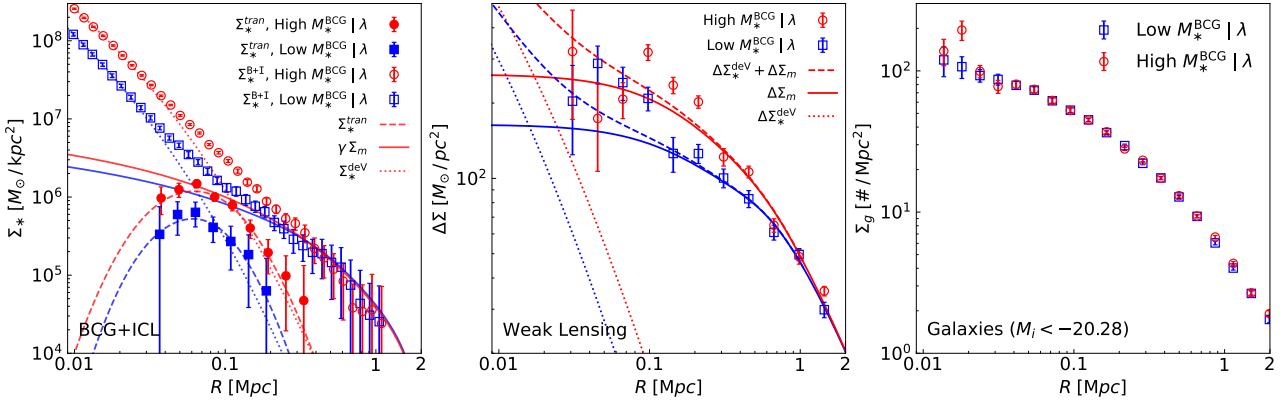


Figure 13. *Left:* BCG+ICL stellar surface density profiles Σ_*^{B+I} of the low (blue open squares) and high (red open circles) M_*^{BCG} subsamples. Solid and dotted curves are the best-fitting scaled matter density and de Vaucouleurs' profiles on relevant scales, respectively. Blue filled squares and red filled circles indicate the transitional components of the low and high- M_*^{BCG} clusters, respectively, while the dashed curves are predictions from the best-fitting Equation 9. *Middle:* Weak lensing profiles $\Delta\Sigma$ of the low (blue open squares) and high (red open circles) M_*^{BCG} subsamples. Solid curves are the predictions by the best-fitting $\Delta\Sigma$ models described in Z21. The two $\Delta\Sigma$ models have the same halo mass, but the average halo concentration of the high- M_*^{BCG} subsample is $\sim 10\%$ higher than that of the low- M_*^{BCG} clusters. Dotted curves indicate the predicted $\Delta\Sigma$ signal induced by the respective de Vaucouleurs' profiles shown in the left panel, and each dashed curve is the sum of the dotted and solid curves of the same colour. *Right:* The galaxy surface number density profiles Σ_g of the low (blue open squares) and high (red open circles) M_*^{BCG} subsamples. The two measured profiles are consistent with each other on all scales.

6 CONCLUSION

In this paper, we have measured the stacked BCG+ICL surface brightness profiles $\mu^{B+I}(R)$ in the SDSS *gri* bands for a sample of ~ 3000 clusters detected between $0.2 < z < 0.3$ from SDSS DR8 imaging. Adopting an empirically calibrated mass-to-light relation, we convert the three-band μ^{B+I} profiles to the diffuse stellar surface density profile $\Sigma_*^{B+I}(R)$. By comparing the Σ_*^{B+I} profile with the cluster weak lensing profile, we find that the ICL on scales $R > 400$ kpc can be well described by the projected dark matter density profile Σ_m multiplied by the ICL-to-halo mass ratio of 1/675.

Further assuming that the inner BCG follows the de Vaucouleurs' law, we develop a physically-motivated method to decompose $\Sigma_*^{B+I}(R)$ into three components, including an inner de Vaucouleurs' profile, an outer ICL that follows the dark matter, and a third excess component at the transitional scales between 70 kpc and 200 kpc. We find that the ratio between this transitional component Σ_*^{tran} and $\Sigma_*^{B+I}(R)$ can be well described by a Gaussian function that peaks at $R_t = 116$ kpc with a logarithmic dispersion of $\sigma_t = 0.23$ dex. After correcting for mask incompleteness using the conditional stellar mass function of satellites measured by Yang et al. (2012), we infer the stellar mass budget of the clusters in three states as: the BCG (8.4%; de Vaucouleurs + transitional), the satellites (83.5%), and the diffuse ICL that follows the dark matter distribution (8.1%). By measuring the weak lensing halo mass as $2.57 \times 10^{14} M_\odot$, the stellar-to-halo mass fractions are 1.531% (satellites), 0.155% (BCG), and 0.148% (ICL), leading to a total stellar-to-halo fraction of 1.834%.

The transitional component Σ_*^{tran} is the key to solving the radius of the BCG sphere of influence R_{SOI} in the diffuse cluster light — R_{SOI} could be well within $R_t \times 10^{-\sigma_t} \sim 70$ kpc if Σ_*^{tran} is induced by the interaction between satellite galaxies and the cluster potential, or extend to $R_t \times 10^{\sigma_t} \sim 200$ kpc if Σ_*^{tran} is tied to the BCG growth. To distinguish the two physical scenarios, we divide the clusters into two subsamples by their BCG stellar mass M_*^{BCG} (with an effective aperture of ~ 50 kpc) at fixed satellite richness λ , and compare their BCG+ICL surface brightness and stellar density profiles. Surprisingly, we discover that the two Σ_*^{B+I} profiles differ

significantly on all scales below $R \sim 200$ kpc, before converging to the same amplitude on larger scales.

From the weak lensing and cluster-galaxy cross-correlations in Z21, we show that the two subsamples have the same average halo mass as well as the same satellite number density profile, but differ only in their average BCG stellar mass. Therefore, the observed discrepancy between the two Σ_*^{B+I} profiles signals a detection of the BCG sphere of influence at $R_{SOI} \approx 200$ kpc. We test the sensitivity of our experiment to the aperture size of stellar mass measurements as well as the miscentring effect of the optical clusters, and demonstrate that $R_{SOI} \approx 200$ kpc is robust against the two systematic uncertainties in the experiment.

Weak lensing measurements also suggest that the high- M_*^{BCG} clusters are $\sim 10\%$ more concentrated than their low- M_*^{BCG} counterparts, suggesting that R_{SOI} is likely connected to the characteristic scale r_s of the NFW haloes. We speculate that the relatively high escape velocity profile within r_s may help confine the stray stars that break free of the BCGs, producing the excess mass at the transitional scales (Kelson 2002; Bender 2015; Veale 2018). Detailed kinematic analysis of the hydrodynamical simulations of cluster formation could be tremendously helpful for providing insight to the growth of the BCG sphere of influence, as well as an indirect check of the physical link between r_s and R_{SOI} . Observationally, our work can be easily extended to the larger cluster catalogues (Zou et al. 2021; Wen & Han 2021; Yang et al. 2021) and deeper photometry (Huang et al. 2021; Li et al. 2021) from current stage-III imaging surveys. Future ground-based and space missions like the LSST, Euclid, Roman, and CSST with even larger cluster samples, deeper photometry, and sharper shear measurements will greatly enhance our capability of seeing cluster formation through the diffuse light.

DATA AVAILABILITY

The data underlying this article will be shared on reasonable request to the corresponding author.

ACKNOWLEDGEMENTS

We thank Weiguang Cui, Fengshan Liu, Zhonglue Wen, and Hu Zou for helpful discussions. Y.Z. acknowledges the support by the National Key Basic Research and Development Program of China (No. 2018YFA0404504), National Science Foundation of China (11873038, 11621303, 11890692, 12173024), and the science research grants from the China Manned Space Project (No. CMS-CSST-2021-A01, CMS-CSST-2021-B01). Y.Z. acknowledges the National One-Thousand Youth Talent Program of China, the SJTU start-up fund (No. WF220407220), and the support by the 111 Project of the Ministry of Education under grant No. B20019. H.S. acknowledges the support from CMS-CSST-2021-A01, NSFC of China under grant 11973070, the Shanghai Committee of Science and Technology grant No.19ZR1466600, and Key Research Program of Frontier Sciences, CAS, Grant No. ZDBS-LY-7013. X.C. acknowledges the hospitality of Zhejiang University where he enjoyed a fruitful discussion with participants of the 23rd “Guoshoujing Meeting on Galaxy Formation and Cosmology”.

REFERENCES

- Aihara H., et al., 2011, *ApJS*, **193**, 29
 Alonso Asensio I., Dalla Vecchia C., Bahé Y. M., Barnes D. J., Kay S. T., 2020, *MNRAS*, **494**, 1859
 Arnaboldi M., Freeman K. C., Mendez R. H., Capaccioli M., Ciardullo R., Ford H., Gerhard O., et al., 1996, *ApJ*, **472**, 145. doi:10.1086/178050
 Bender, *Ralf and Kormendy, John and Cornell, Mark E. and Fisher, David B.* *ApJ*, **807**, 56
 Bernardi M., Meert A., Sheth R. K., Vikram V., Huertas-Company M., Mei S., Shankar F., 2013, *MNRAS*, **436**, 697
 Bernardi, *M. and Meert, A. and Sheth, R. K. and Fischer, J. -L. and Huertas-Company, M. and Maraston, C. and Shankar, F. and Vikram, V.* *MNRAS*, **467**, 2217
 Bertin E., Arnouts S., 1996, *A&AS*, **117**, 393
 Blanton M. R., Kazin E., Muna D., Weaver B. A., Price-Whelan A., 2011, *AJ*, **142**, 31
 Burke C., Collins C. A., Stott J. P., Hilton M., 2012, *MNRAS*, **425**, 2058
 Burke C., Hilton M., Collins C., 2015, *MNRAS*, **449**, 2353
 Chen Y.-M., et al., 2012, *MNRAS*, **421**, 314
 Contini E., 2021, *Galaxies*, **9**, 60
 Contini E., De Lucia G., Villalobos Á., Borgani S., 2014, *MNRAS*, **437**, 3787
 Contini E., Yi S. K., Kang X., 2018, *MNRAS*, **479**, 932
 Contini E., Yi S. K., Kang X., 2019, *ApJ*, **871**, 24
 Cooper A. P., Gao L., Guo Q., Frenk C. S., Jenkins A., Springel V., White S. D. M., 2015, *MNRAS*, **451**, 2703
 Cui W., et al., 2014, *MNRAS*, **437**, 816
 DeMaio T., Gonzalez A. H., Zabludoff A., Zaritsky D., Bradač M., 2015, *MNRAS*, **448**, 1162
 DeMaio T., Gonzalez A. H., Zabludoff A., Zaritsky D., Connor T., Donahue M., Mulchaey J. S., 2018, *MNRAS*, **474**, 3009
 de Vaucouleurs G., de Vaucouleurs A., 1970, *ApL*, **5**, 219
 Dey A., Schlegel D. J., Lang D., Blum R., Burleigh K., Fan X., Findlay J. R., et al., 2019, *AJ*, **157**, 168. doi:10.3847/1538-3881/ab089d
 Doherty M., Arnaboldi M., Das P., Gerhard O., Aguerri J. A. L., Ciardullo R., Feldmeier J. J., et al., 2009, *A&A*, **502**, 771. doi:10.1051/0004-6361/200811532
 Dolag K., Murante G., Borgani S., 2010, *MNRAS*, **405**, 1544
 Donzelli C. J., Muriel H., Madrid J. P., 2011, *ApJS*, **195**, 15
 D’Souza, *Richard and Kauffman, Guinevere and Wang, Jing and Vegetti, Simona* *MNRAS*, **443**, 1443
 Efron B., Stein C., 1981, *The Annals of Statistics*, **9**, 586
 Feldmeier J. J., Mihos J. C., Morrison H. L., Harding P., Kaib N., Dubinski J., 2004, *ApJ*, **609**, 617. doi:10.1086/421313
 Furnell K. E., et al., 2021, *MNRAS*, **502**, 2419
 Gong Y., et al., 2019, *ApJ*, **883**, 203
 Gonzalez A. H., Zabludoff A. I., Zaritsky D., 2005, *ApJ*, **618**, 195
 Gu M., et al., 2020, *ApJ*, **894**, 32
 Hollowood D. L., et al., 2019, *ApJS*, **244**, 22
 Huang S., et al., 2021, arXiv e-prints, p. arXiv:2109.02646
 Infante-Sainz, *Raúl and Trujillo, Ignacio and Román, Javier*, 2020, *MNRAS*, **491**, 5317
 Ivezić Ž., et al., 2019, *ApJ*, **873**, 111
 Jiménez-Teja Y., et al., 2018, *ApJ*, **857**, 79
 Jiménez-Teja Y., et al., 2019, *A&A*, **622**, A183
 Johnston D. E., et al., 2007, arXiv e-prints, p. arXiv:0709.1159
 Kelson, *Daniel D. and Zabludoff, Ann I. and Williams, K. A. and Trager, S. C. and Mulchaey, J. S. and Bolte, Michael* *ApJ*, **576**, 720
 Kluge M., Bender R., Riffeser A., Goessl C., Hopp U., Schmidt M., Ries C., 2021, *ApJS*, **252**, 27
 Koester B. P., McKay T. A., Annis J., Wechsler R. H., Evrard A., Bleem L., Becker M., et al., 2007, *ApJ*, **660**, 239. doi:10.1086/509599
 Kormendy J., Bahcall J. N., 1974, *AJ*, **79**, 671. doi:10.1086/111595
 Kravtsov A. V., Vikhlinin A. A., Meshcheryakov A. V., 2018, *Astronomy Letters*, **44**, 8
 Krick J. E., Bernstein R. A., 2007, *AJ*, **134**, 466. doi:10.1086/518787
 Laureijs R., Amiaux J., Arduini S., Auguères J.-L., Brinchmann J., Cole R., Cropper M., et al., 2011, arXiv, arXiv:1110.3193
 Li J., Huang S., Leauthaud A., Moustakas J., Danieli S., Greene J. E., Abraham R., et al., 2021, arXiv, arXiv:2111.03557
 Longobardi A., Arnaboldi M., Gerhard O., Hanuschik R., 2015, *A&A*, **579**, A135. doi:10.1051/0004-6361/201525773
 Mancone C. L., Gonzalez A. H., 2012, *PASP*, **124**, 606
 Maraston C., Strömbäck G., Thomas D., Wake D. A., Nichol R. C., 2009, *MNRAS*, **394**, L107
 Martel H., Barai P., Brito W., 2012, *ApJ*, **757**, 48
 Melnick J., White S. D. M., Hoessel J., 1977, *MNRAS*, **180**, 207. doi:10.1093/mnras/180.2.207
 Melnick J., Giraud E., Toledo I., Selman F., Quintana H., 2012, *MNRAS*, **427**, 850
 Mihos J. C., Harding P., Feldmeier J., Morrison H., 2005, *ApJ*, **631**, L41
 Montes M., Trujillo I., 2014, *ApJ*, **794**, 137
 Montes M., Trujillo I., 2018, *MNRAS*, **474**, 917
 Montes M., Trujillo I., 2019, *MNRAS*, **482**, 2838
 Contini E., Gu Q., 2020, *ApJ*, **901**, 128
 Montes M., Brough S., Owers M. S., Santucci G., 2021, *ApJ*, **910**, 45
 Morishita T., Abramson L. E., Treu T., Schmidt K. B., Vulcani B., Wang X., 2017, *ApJ*, **846**, 139
 Murante G., Giovanlli M., Gerhard O., Arnaboldi M., Borgani S., Dolag K., 2007, *MNRAS*, **377**, 2
 Navarro J. F., Frenk C. S., White S. D. M., 1997, *ApJ*, **490**, 493. doi:10.1086/304888
 Oguri M., Takada M., 2011, *Phys. Rev. D*, **83**, 023008
 Planck Collaboration et al., 2016, *A&A*, **594**, A13
 Presotto V., et al., 2014, *A&A*, **565**, A126
 Puchwein E., Springel V., Sijacki D., Dolag K., 2010, *MNRAS*, **406**, 936
 Purcell C. W., Bullock J. S., Zentner A. R., 2007, *ApJ*, **666**, 20
 Rozo E., Rykoff E. S., 2014, *ApJ*, **783**, 80
 Romanowsky A. J., Strader J., Brodie J. P., Mihos J. C., Spitler L. R., Forbes D. A., Foster C., et al., 2012, *ApJ*, **748**, 29. doi:10.1088/0004-637X/748/1/29
 Rudick C. S., Mihos J. C., McBride C., 2006, *ApJ*, **648**, 936
 Rudick C. S., Mihos J. C., Frey L. H., McBride C. K., 2009, *ApJ*, **699**, 1518
 Rudick C. S., Mihos J. C., McBride C. K., 2011, *ApJ*, **732**, 48
 Rykoff E. S., et al., 2014, *ApJ*, **785**, 104
 Rykoff E. S., et al., 2016, *ApJS*, **224**, 1
 Sampaio-Santos H., Zhang Y., Ogando R. L. C., Shin T., Golden-Marx J. B., Yanny B., Herner K., et al., 2021, *MNRAS*, **501**, 1300. doi:10.1093/mnras/staa3680
 Seigar M. S., Graham A. W., Jerjen H., 2007, *MNRAS*, **378**, 1575
 Simet M., McClintock T., Mandelbaum R., Rozo E., Rykoff E., Sheldon E., Wechsler R. H., 2017, *MNRAS*, **466**, 3103

Sommer-Larsen J., 2006, MNRAS, 369, 958. doi:10.1111/j.1365-2966.2006.10352.x

Spergel D., et al., 2015, arXiv e-prints, p. arXiv:1503.03757

Spinello C., Napolitano N. R., Arnaboldi M., Tortora C., Coccato L., Capaccioli M., Gerhard O., et al., 2018, MNRAS, 477, 1880. doi:10.1093/mnras/sty663

Tal, Tomer and van Dokkum, Pieter G. ApJ, 731, 89

Tang L., Lin W., Cui W., Kang X., Wang Y., Contini E., Yu Y., 2018, ApJ, 859, 85

Veale, Melanie and Ma, Chung-Pei and Greene, Jenny E. and Thomas, Jens and Blakeslee, John P. and Walsh, Jonelle L. and Ito, Jennifer MNRAS, 473, 5446

Wang, Wenting and Han, Jiaxin and Sonnenfeld, Alessandro and Yasuda, Naoki and Li, Xiangchong and Jing, Yipeng and More, Surhud and Price, Paul A. and Lupton, Robert and Rykoff, Eli S. and Stark, David V. and Lan, Ting-Wen and Takada, Masahiro and Huang, Song and Luo, Wentao and Bahcall, Neta A. and Komiyama, Yutaka MNRAS, 487, 1580

Wang, Wenting and Li, Xiangchong and Shi, Jingjing and Han, Jiaxin and Yasuda, Naoki and Jing, Yipeng and More, Surhud and Takada, Masahiro and Miyatake, Hironao and Nishizawa, Atsushi J. ApJ, 919, 25

Welch G. A., Sastry G. N., 1971, ApJL, 169, L3. doi:10.1086/180801

Wen Z. L., Han J. L., 2021, MNRAS, 500, 1003. doi:10.1093/mnras/staa3308

Wetzel A. R., White M., 2010, MNRAS, 403, 1072. doi:10.1111/j.1365-2966.2009.16191.x

Willman B., Governato F., Wadsley J., Quinn T., 2004, MNRAS, 355, 159

Yang X., Mo H. J., van den Bosch F. C., Zhang Y., Han J., 2012, ApJ, 752, 41

Yang X., Xu H., He M., Gu Y., Katsianis A., Meng J., Shi F., et al., 2021, ApJ, 909, 143. doi:10.3847/1538-4357/abddb2

York D. G., et al., 2000, AJ, 120, 1579

Zhang Y., et al., 2019, ApJ, 874, 165

Zibetti S., White S. D. M., Schneider D. P., Brinkmann J., 2005, MNRAS, 358, 949

Zou H., Gao J., Xu X., Zhou X., Ma J., Zhou Z., Zhang T., et al., 2021, ApJS, 253, 56. doi:10.3847/1538-4365/abe5b0

Zu Y., Mandelbaum R., 2015, MNRAS, 454, 1161. doi:10.1093/mnras/stv2062

Zu Y., Mandelbaum R., Simet M., Rozo E., Rykoff E. S., 2017, MNRAS, 470, 551. doi:10.1093/mnras/stx1264

Zu Y., et al., 2021a, MNRAS, 505, 5117

Zu Y., et al., 2021b, arXiv e-prints, 2022, MNRAS, 511, 1789

Zwicky F., 1937, ApJ, 86, 217

This paper has been typeset from a TeX/LaTeX file prepared by the author.